

Chapter 5

Calorimetry

5.1 Introduction

An overview of the ATLAS calorimetry system [104, 105] is given in section 1.3. The overall system is depicted in figure 1.3, its general performance goals are listed in table 1.1, and its main parameters are given in table 1.3.

The ATLAS calorimeters consist of a number of sampling detectors with full ϕ -symmetry and coverage around the beam axis. The calorimeters closest to the beam-line are housed in three cryostats, one barrel and two end-caps. The barrel cryostat contains the electromagnetic barrel calorimeter, whereas the two end-cap cryostats each contain an electromagnetic end-cap calorimeter (EMEC), a hadronic end-cap calorimeter (HEC), located behind the EMEC, and a forward calorimeter (FCal) to cover the region closest to the beam. All these calorimeters use liquid argon as the active detector medium; liquid argon has been chosen for its intrinsic linear behaviour, its stability of response over time and its intrinsic radiation-hardness.

The precision electromagnetic calorimeters are lead-liquid argon detectors with accordion-shape absorbers and electrodes. This geometry allows the calorimeters to have several active layers in depth, three in the precision-measurement region ($0 < |\eta| < 2.5$) and two in the higher- η region ($2.5 < |\eta| < 3.2$) and in the overlap region between the barrel and the EMEC. In the precision-measurement region, an accurate position measurement is obtained by finely segmenting the first layer in η . The η -direction of photons is determined by the position of the photon cluster in the first and the second layers. The calorimeter system also has electromagnetic coverage at higher η ($3.1 < |\eta| < 4.9$) provided by the FCal. Furthermore in the region ($0 < |\eta| < 1.8$) the electromagnetic calorimeters are complemented by presamplers, an instrumented argon layer, which provides a measurement of the energy lost in front of the electromagnetic calorimeters.

For the outer hadronic calorimeter, the sampling medium consists of scintillator tiles and the absorber medium is steel. The tile calorimeter is composed of three parts, one central barrel and two extended barrels. The choice of this technology provides maximum radial depth for the least cost for ATLAS. The tile calorimeter covers the range $0 < |\eta| < 1.7$ (central barrel and extended barrels). The hadronic calorimetry is extended to larger pseudorapidities by the HEC, a copper/liquid-argon detector, and the FCal, a copper-tungsten/liquid-argon detector. The hadronic calorimetry thus reaches one of its main design goals, namely coverage over $|\eta| < 4.9$.

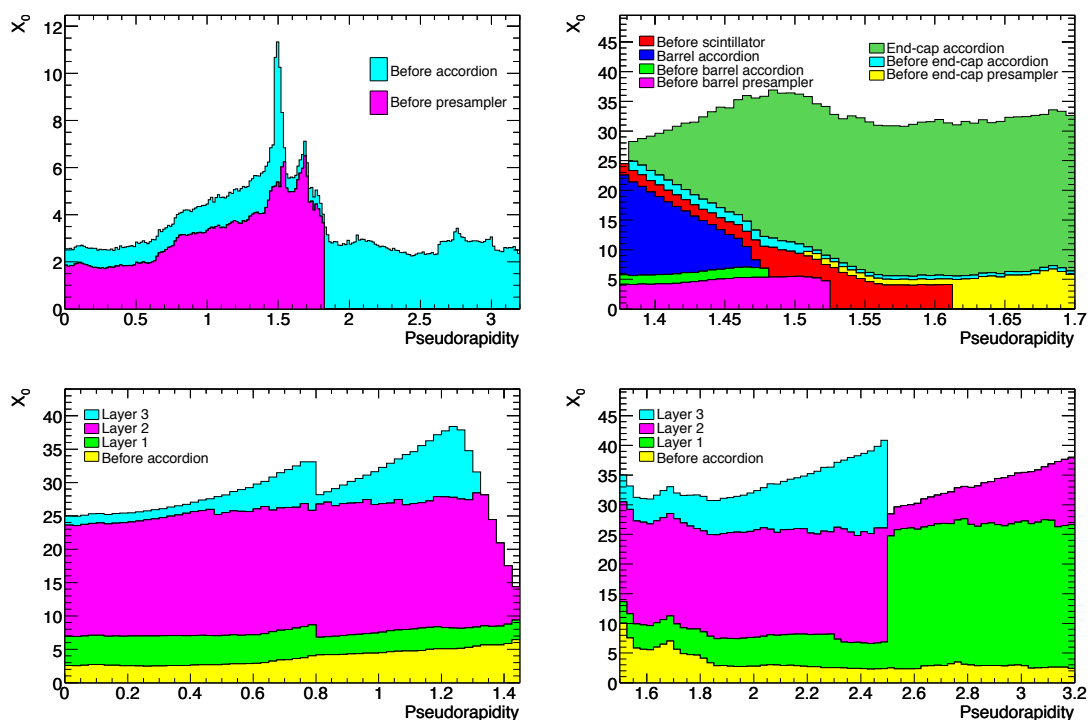


Figure 5.1: Cumulative amounts of material, in units of radiation length X_0 and as a function of $|\eta|$, in front of and in the electromagnetic calorimeters. The top left-hand plot shows separately the total amount of material in front of the presampler layer and in front of the accordion itself over the full η -coverage. The top right-hand plot shows the details of the crack region between the barrel and end-cap cryostats, both in terms of material in front of the active layers (including the crack scintillator) and of the total thickness of the active calorimeter. The two bottom figures show, in contrast, separately for the barrel (left) and end-cap (right), the thicknesses of each accordion layer as well as the amount of material in front of the accordion.

The numbers of radiation and interaction lengths in front of and in the electromagnetic and hadronic calorimeters are shown in figures 5.1 and 5.2.

Sections 5.2 and 5.3 are devoted to the description of the electromagnetic and hadronic calorimetry, respectively. Section 5.4 describes the LAr cryostats and feed-throughs. The instrumentation in the gaps between the cryostats is described in section 5.5. The front-end read-out electronics, back-end electronics and services are described in section 5.6. Finally, test-beam measurements obtained with production modules of the different calorimeters are presented in section 5.7.

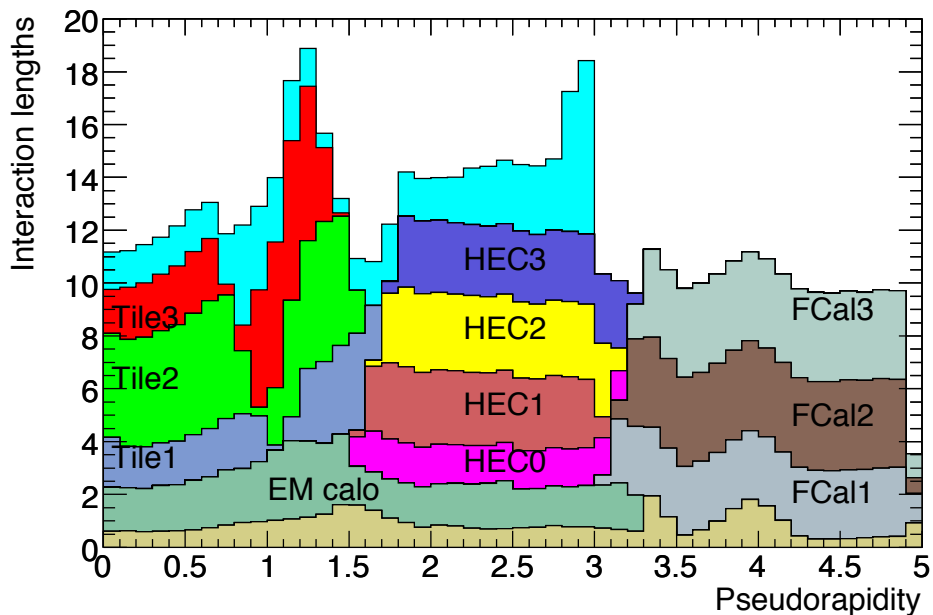


Figure 5.2: Cumulative amount of material, in units of interaction length, as a function of $|\eta|$, in front of the electromagnetic calorimeters, in the electromagnetic calorimeters themselves, in each hadronic layer, and the total amount at the end of the active calorimetry. Also shown for completeness is the total amount of material in front of the first active layer of the muon spectrometer (up to $|\eta| < 3.0$).

5.2 Electromagnetic calorimetry

5.2.1 Accordion geometry

An accordion geometry has been chosen for the absorbers and the electrodes of the barrel and end-cap electromagnetic calorimeters (see figures 5.3 and 5.4). Such a geometry provides naturally a full coverage in ϕ without any cracks, and a fast extraction of the signal at the rear or at the front of the electrodes. In the barrel, the accordion waves are axial and run in ϕ , and the folding angles of the waves vary with radius to keep the liquid-argon gap constant (see figures 5.4 and 5.5). In the end-caps, the waves are parallel to the radial direction and run axially. Since the liquid-argon gap increases with radius in the end-caps, the wave amplitude and the folding angle of the absorbers and electrodes vary with radius (see figure 5.6). All these features of the accordion geometry lead to a very uniform performance in terms of linearity and resolution as a function of ϕ . As can be seen from figure 5.3, the first layer is finely segmented along η , as for example in the barrel where there are eight strips in front of a middle cell. One can note however the coarser granularity of the first layer in the edge zones of the barrel and end-caps, as explicitly given in table 1.3. The second layer collects the largest fraction of the energy of the electromagnetic shower, and the third layer collects only the tail of the electromagnetic shower and is therefore less segmented in η .

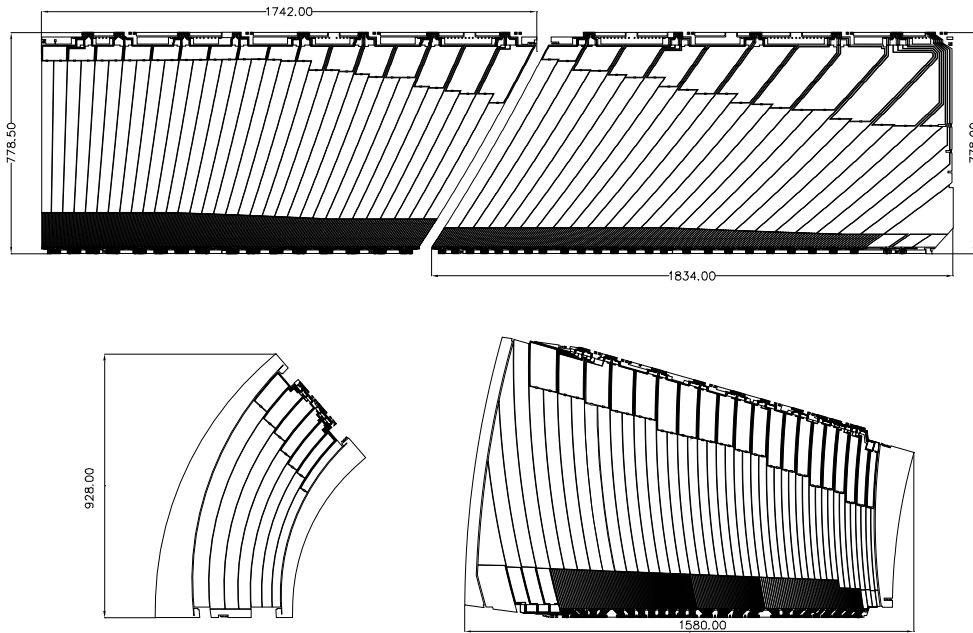


Figure 5.3: Layout of the signal layer for the four different types of electrodes before folding. The two top electrodes are for the barrel and the two bottom electrodes are for the end-cap inner (left) and outer (right) wheels. Dimensions are in millimetres. The drawings are all at the same scale. The two or three different layers in depth are clearly visible.

The absorbers are made of lead plates, to which two stainless-steel sheets (0.2 mm thick) are glued using a resin-impregnated glass-fibre fabric to provide mechanical strength. The lead plates in the barrel have a thickness of 1.53 mm for $|\eta| < 0.8$ and of 1.13 mm for $|\eta| > 0.8$. The change in lead thickness at $|\eta| = 0.8$ limits the decrease of the sampling fraction as $|\eta|$ increases. In the end-cap calorimeters, the plates have a thickness of 1.7 mm for $|\eta| < 2.5$ and of 2.2 mm for $|\eta| > 2.5$.

The readout electrodes [106] are located in the gaps between the absorbers and consist of three conductive copper layers separated by insulating polyimide sheets. The two outer layers are at the high-voltage potential and the inner one is used for reading out the signal via capacitive coupling. The segmentation of the calorimeter in η and in depth is obtained by etched patterns on the different layers, as shown in figure 5.3. The ϕ -segmentation is obtained by ganging together the appropriate number of electrodes (see section 5.2.6). Each barrel gap between two absorbers is equipped with two electrodes, one type for $|\eta| < 0.8$ and another for $|\eta| > 0.8$. Similarly, each end-cap gap between two absorbers is equipped with one type of electrode for $|\eta| < 2.5$ and with another for $|\eta| > 2.5$.

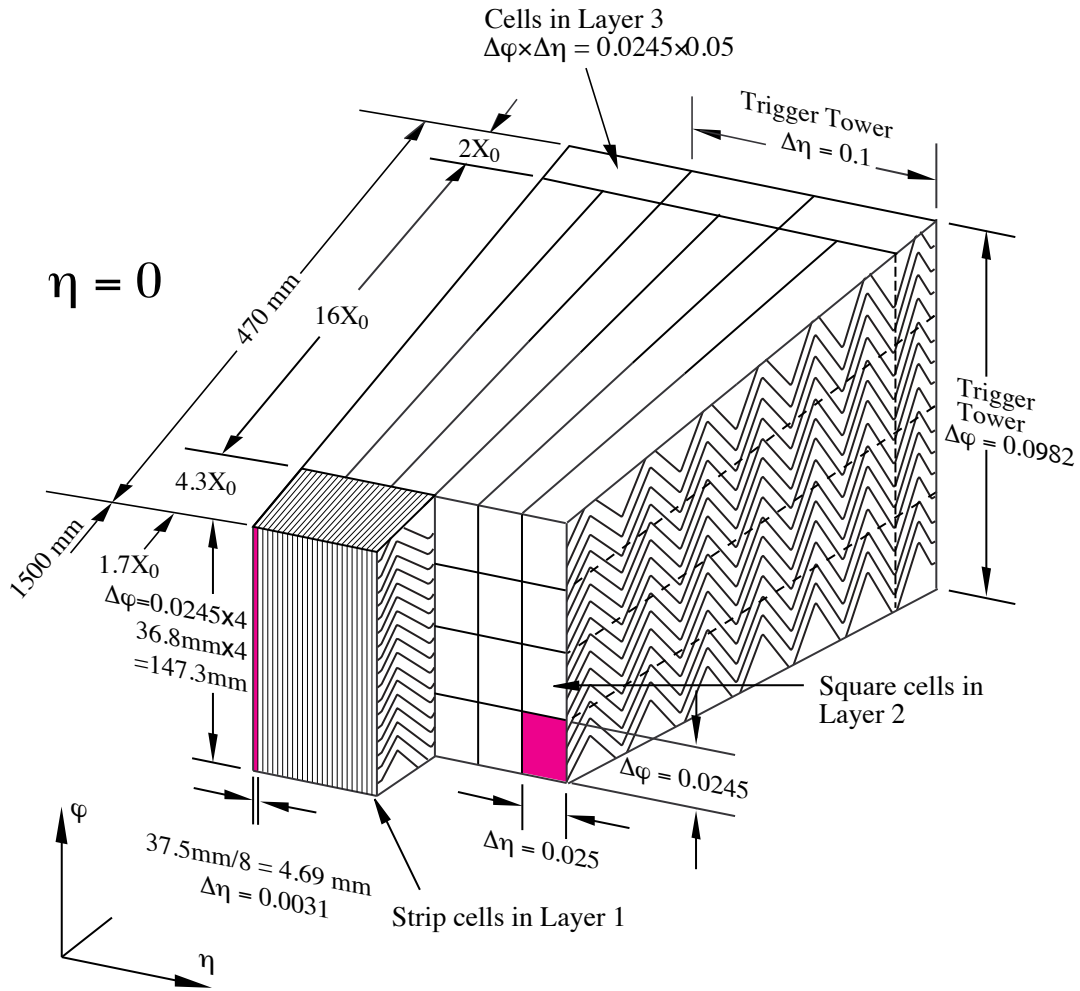


Figure 5.4: Sketch of a barrel module where the different layers are clearly visible with the ganging of electrodes in ϕ . The granularity in η and ϕ of the cells of each of the three layers and of the trigger towers is also shown.

5.2.2 Barrel geometry

The barrel electromagnetic calorimeter [107] is made of two half-barrels, centred around the z -axis. One half-barrel covers the region with $z > 0$ ($0 < \eta < 1.475$) and the other one the region with $z < 0$ ($-1.475 < \eta < 0$). The length of each half-barrel is 3.2 m, their inner and outer diameters are 2.8 m and 4 m respectively, and each half-barrel weighs 57 tonnes. As mentioned above, the barrel calorimeter is complemented with a liquid-argon presampler detector, placed in front of its inner surface, over the full η -range.

A half-barrel is made of 1024 accordion-shaped absorbers, interleaved with readout electrodes. The electrodes are positioned in the middle of the gap by honeycomb spacers. The size of the drift gap on each side of the electrode is 2.1 mm, which corresponds to a total drift time of about 450 ns for an operating voltage of 2000 V. Once assembled, a half-barrel presents no



Figure 5.5: Photograph of a partly stacked barrel electromagnetic LAr module. A total of six out of seven outer support rings into which the absorbers can be seen. The backbone behind the outer support rings and the assembly bench below the stacked modules are also visible.



Figure 5.6: Photograph showing a side view of an electromagnetic end-cap LAr module (the beam axis is vertical). The first accordion absorber of each wheel is clearly visible, as well as the summing boards, the motherboards and the cables.

discontinuity along the azimuthal angle ϕ ; however, for ease of construction, each half-barrel has been divided into 16 modules, each covering a $\Delta\phi = 22.5^\circ$. The total thickness of a module is at least 22 radiation lengths (X_0), increasing from 22 X_0 to 30 X_0 between $|\eta| = 0$ and $|\eta| = 0.8$ and from 24 X_0 to 33 X_0 between $|\eta| = 0.8$ and $|\eta| = 1.3$.

At the inner and outer edges, each absorber is encased in the groove of a precision-machined glass-fibre composite bar. The purpose of these bars is to accurately position each absorber with respect to its neighbours and also to provide space for the connectors of the electrodes. The stacking of these bars defines the cylindrical geometry of the half-barrel.

Seven stainless-steel outer rings support a half-barrel and provide it with the required rigidity. Each ring is made of 16 ring-pieces corresponding to the 16 modules. All ring-pieces are identical with an I-beam cross-section except for the two ring-pieces at the level of the cryostat rails. Similarly, eight composite inner rings define the inner geometry of a half-barrel. Each inner ring is also made of 16 identical ring-pieces. The absorber bars are screwed into these ring-pieces.

A module, as depicted in figures 5.4 and 5.5, has three layers or layers in depth (front, middle and back as viewed from the interaction point). The front layer is read out at the low-radius side of the electrode, whereas the middle and back layers are read out at the high-radius side of the electrode. The readout granularity of the different layers is shown in table 1.3. In total, there are 3424 readout cells per module, including the presampler cells. The amount of dead material in front of the presampler and between the presampler and the first calorimeter layer as well as the thickness of each calorimeter layer are shown in figure 5.1 in units of X_0 .

The presampler [108] is a separate thin liquid-argon layer (11 mm in depth), which provides shower sampling in front of the active electromagnetic calorimeter and inside the barrel cryostat. This presampler layer is made of 64 identical azimuthal sectors (32 per half-barrel). Each sector is 3.1 m long and 0.28 m wide, thus covering the half-barrel length and providing a coverage in $\Delta\eta \times \Delta\phi$ of 1.52×0.2 . It is composed of eight modules of different size, with a length increasing

with $|\eta|$ to obtain a constant η -granularity of $\Delta\eta = 0.2$ for each module, except for the module at the end of the barrel, for which the η -coverage is reduced to 0.12.

The presampler modules are made of interleaved cathode and anode electrodes glued between glass-fibre composite plates. The electrode spacing varies slightly, from 1.9 to 2.0 mm, with the presampler module type. The cathodes are double-sided printed-circuit boards while the anodes have three conductive layers separated by glass-fibre composite layers. The required segmentation, $\Delta\eta \sim 0.025$ and $\Delta\phi = 0.1$, for each module is obtained by ganging the appropriate number of anodes in the η direction and by subdividing (i.e. etching) each anode into two halves in the ϕ -direction. A high voltage potential of +2 kV is applied to the outer layers of the anodes and the signal is read out through capacitive coupling to the central layer at ground potential.

5.2.3 End-cap geometry

The EMEC calorimeters [109] consist of two wheels, one on each side of the electromagnetic barrel. Each wheel is 63 cm thick and weighs 27 tonnes, with external and internal radii at ambient temperature of 2098 mm and 330 mm, respectively. It covers the region $1.375 < |\eta| < 3.2$. In the transition region between the barrel and the end-cap calorimeters, the material in front of the calorimeter amounts to several X_0 , as shown in figure 5.1. In order to improve the energy measurement in this region, a liquid-argon presampler is implemented in front of the end-cap calorimeter, covering the range $1.5 < |\eta| < 1.8$.

Each end-cap calorimeter consists itself of two co-axial wheels. The boundary between the inner and the outer wheel, which is 3 mm wide and located at $|\eta| = 2.5$, is mostly filled with low-density material. This boundary is approximately projective and matches the acceptance of the inner detector (see figure 4.1). Each end-cap wheel is further divided into eight wedge-shaped modules without introducing any discontinuity along the azimuthal angle owing to the accordion geometry. A view of a module is shown in figure 5.6. Each end-cap contains 768 absorbers interleaved with readout electrodes in the outer wheel and 256 absorbers in the inner wheel. The electrodes are positioned in the middle of the gaps by honeycomb spacers. The total active thickness of an end-cap calorimeter is greater than $24 X_0$ except for $|\eta| < 1.475$. The thickness increases from 24 to $38 X_0$ as $|\eta|$ increases from 1.475 to 2.5 (outer wheel) and from 26 to $36 X_0$ as $|\eta|$ increases from 2.5 to 3.2 (inner wheel). The calorimeter support frame is composed of six support rings: three on the front (at three different radii) and three on the back. The total weight of the detector is supported mainly by the rings at the largest radius.

In the outer wheel, signals from the different pads are read out from both sides of the electrode, as in the case of the barrel electromagnetic calorimeter. In the inner wheel, because of the higher radiation levels, the signals are all read out from the back side.

As for the barrel electromagnetic calorimeter, the precision region in the end-cap electromagnetic calorimeters ($1.5 < |\eta| < 2.5$) is divided in depth into three longitudinal layers. The front layer, about $4.4 X_0$ thick, is segmented with strips along the η direction. The transverse size of the projective cell in the middle layer is the same as defined in the barrel electromagnetic calorimeter, $\Delta\eta \times \Delta\phi = 0.025 \times 0.025$. The back layer has a twice coarser granularity in η . The outermost region $|\eta| < 1.5$ of the outer wheel and the inner wheel ($2.5 < |\eta| < 3.2$) are segmented in only two longitudinal layers and have a coarser transverse granularity. Table 1.3 summarises the

longitudinal and transverse readout granularities of the electromagnetic end-cap calorimeter as a function of $|\eta|$. The η -granularity in the front layer varies with η in order to keep the copper strip width larger than a few mm (see table 1.3). The ϕ -granularity is obtained by ganging the signals from adjacent electrodes (see section 5.2.6). Each module contains 3984 readout channels, including the 96 channels in the presampler.

Each end-cap presampler consists of 32 identical azimuthal sectors or modules. These are placed in a 5 mm deep cavity in the back of the cryostat cold wall. The granularity of the presampler is $\Delta\eta \times \Delta\phi = 0.025 \times 0.1$. One end-cap presampler module consists of two, 2 mm thick, active liquid argon layers, formed by three electrodes parallel to the front face of the EMEC calorimeter. The electrodes, made from double-sided printed-circuit boards, are separated by honeycomb spacers and glued together at the inner and outer radius with 2 mm thick bars. A negative high voltage is applied to the external electrodes and the signals are read out from the central electrode which is segmented into pads. The same signal, calibration and high-voltage cables as for the end-cap calorimeter are used. Two high-voltage cables feed separately the left and right side of a presampler module.

5.2.4 Shape and placement of the electromagnetic calorimeters

After insertion into the cryostat, the circularity of the barrel electromagnetic calorimeter was measured. The deformation due to its weight can reach up to 3 mm at the top and bottom of each half-barrel and is in fair agreement with the corresponding finite-element calculations [107]. In the cold, the deformation is reduced due to the Archimedes thrust caused by the liquid argon which has a relative density of 1.4. The centres of the fitted inner and outer circles coincide to better than 0.5 mm. Finally, the sagging of the absorbers was measured as a function of the azimuthal angle and a maximum value of 2.5 mm near the horizontal plane was found. The same set of measurements has been performed for both end-caps, once they were in vertical position. The measured deformation was found to be up to 2 mm at the top. The sagging of the absorber plates and the small deformation of the barrel electromagnetic calorimeter will induce some distortions in the position measurements but their impact on the energy resolution is expected to be very small.

Due to difficulties in the positioning of the half-barrels inside the cryostat, both half-barrels when cold are 4 mm too low and laterally displaced by 2 mm with respect to the cryostat axis [107]. Part of the vertical misalignment has been compensated by positioning the cryostat approximately 2 mm higher than originally planned inside the experiment (see section 9.3.2.3). To make room for the inner-detector services, the two end-cap cryostats have been positioned 40 mm away from their nominal position in the z -direction. The projectivity of the geometry of these calorimeters has therefore been slightly degraded.

5.2.5 High-voltage distribution

To provide a measure of redundancy, the two high-voltage sides of each electrode are fed independently. The nominal high-voltage for the barrel electromagnetic calorimeter is 2000 V (see table 5.1). If one side of an electrode is not powered, only half of the signal will be collected. The variation of the signal [110] with high voltage is mainly due to the variation of the drift velocity

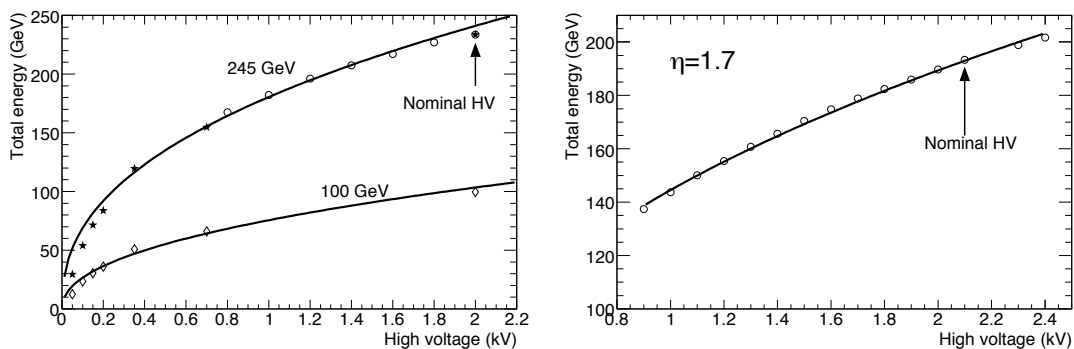


Figure 5.7: Measured electromagnetic cluster energy as a function of the applied high voltage. The results are shown for a barrel module (left), for 245 GeV electrons (open circles), 100 GeV electrons (open diamonds) and for the 100 GeV results at the nominal voltage of 2 kV scaled to the corresponding result at 245 GeV (stars). The results obtained with an end-cap module (right) are shown for 193 GeV electrons. The curves correspond to fits with a functional form $E_{\text{tot}} = a \times V^b$.

with high voltage and is shown in figure 5.7. The variation of the signal amplitude with high voltage is moderate: for example, 77% of the signal is collected when decreasing the high voltage to half of its nominal value. The high-voltage granularity of the barrel electromagnetic calorimeter, including the presampler, is $\Delta\phi \times \Delta\eta = 0.2 \times 0.2$, meaning that 32 electrode sectors are powered simultaneously.

In contrast to the barrel electromagnetic calorimeter, the drift gap on each side of the electrodes is not constant for the EMEC, but is a function of radius and varies from 2.8 mm to 0.9 mm in the outer wheel and from 3.1 mm to 1.8 mm in the inner wheel. To obtain a uniform η -independent detector response, one would therefore need a high voltage continuously varying with η , as illustrated in figure 5.8. In practice, this ideal behaviour is approximated with a variation in steps, also illustrated in figure 5.8. Table 5.1 provides explicitly these nominal high-voltage values as a function of the η -range, thereby defining seven (two) high-voltage sectors for the outer (inner) wheel. The high-voltage granularity is thus 0.2 in ϕ as in the barrel and approximately 0.2 in η , as indicated in table 5.1.

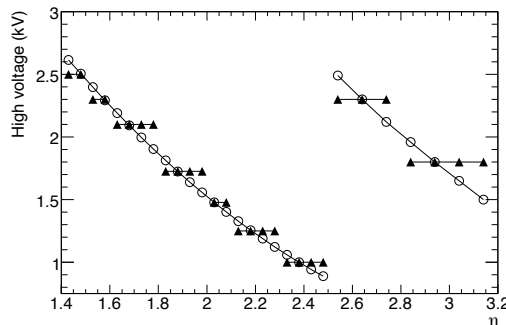


Figure 5.8: High-voltage distribution as a function of $|\eta|$ for the EMEC. A uniform calorimeter response requires a high voltage which varies continuously as a function of $|\eta|$, as shown by the open circles. This has been approximated by a set of discrete values shown as full triangles.

Different solutions have been implemented in case of high-voltage problems. One electrode sector may be powered individually, if the problem was identified at room temperature. On the other hand, if the problem has been identified only in the cryostat when testing individual modules

Table 5.1: Nominal high-voltage settings for the various liquid-argon calorimeter components and as a function of $|\eta|$ in the case of the EMEC outer and inner wheels.

Component	$ \eta $ -range and voltage (V)						
Electromagnetic barrel Voltage	0 – 1.475 +2000						
Electromagnetic end-cap (EMEC) Voltage	1.375 – 1.5 +2500	1.5 – 1.6 +2300	1.6 – 1.8 +2100	1.8 – 2.0 +1700	2.0 – 2.1 +1500	2.1 – 2.3 +1250	2.3 – 2.5 +1000
Electromagnetic end-cap (EMEC) Voltage	2.5 – 2.8 +2300				2.8 – 3.2 +1800		
Barrel presampler Voltage	0 – 1.52 +2000						
End-cap presampler Voltage	1.5 – 1.8 –2000						
Hadronic end-cap (HEC) Voltage	1.5 – 3.2 +1800						
Forward calorimeter FCal1 voltage	3.1 – 4.9 +250						
FCal2 voltage	+375						
FCal3 voltage	+500						

at liquid-argon temperature, one high-voltage sector may be divided into two halves, for example $\Delta\phi \times \Delta\eta = 0.1 \times 0.2$ in the barrel, and the two halves are powered separately. The effect of not supplying high voltage at all to one side of the electrode was studied in the test-beam to verify the expected factor of two loss in signal. A slight deviation from this expectation was observed for the measured signal amplitude at the transition region with a good sector and this was understood as a geometrical effect, which is easy to correct for since it is well reproduced by simulation. An alternative for sector sides with a permanent short is to supply them with high-voltage modules permitting large DC current draws of up to 3 mA, which is in general sufficient to operate the faulty sector at 1000 V or above.

5.2.6 Electronic boards and cables inside the cryostats

The first layer of each calorimeter is read out from the front (inner radius for the barrel electromagnetic calorimeter and small- $|z|$ face for the EMEC), whereas the second and third layers are read out from the back (outer radius for the barrel electromagnetic calorimeter and large- $|z|$ face for the EMEC). The readout is accomplished by several interconnected boards. These include summing boards which generate analogue sums from adjacent calorimeter gaps and mother-boards for analogue sum readout and for distribution of the calibration pulses.

The summing boards are connected to the electrode connectors grouping the signals in ϕ . For the barrel electromagnetic calorimeter and the outer EMEC wheel, each summing board services respectively 16 and 12 electrodes (corresponding to $\Delta\phi = 0.1$). For the first layer, all electrodes are summed into one readout cell, while for the second and third layers they are summed in four adjacent readout cells ($\Delta\phi = 0.025$). For the inner EMEC wheel, each summing board services eight electrodes ($\Delta\phi = 0.2$) and for each of the two layers, four adjacent electrodes are summed to form readout cells ($\Delta\phi = 0.1$).

A mother-board provides readout for a $\Delta\eta \times \Delta\phi$ region of size 0.2×0.2 . The receptacles at the output of the summing boards and the input of the mother-boards are connected via pins mounted on two thin printed-circuit boards. Each channel is connected twice to provide maximum robustness and redundancy. For the second and third calorimeter layers, every other printed-circuit board also houses a low-capacitance transient voltage suppressor [107], referenced to ground, with a turn-on at 6 V to protect against accidental discharges, which might damage the calibration resistors mounted on the mother-board. The mother-boards route the outputs to the readout cables through a connector designed to minimise cross-talk between readout channels. The mother-boards also include surface-mounted 0.1% tolerance tantalum-nitride calibration resistors (non-hygroscopic with a temperature coefficient of 70 ± 5 ppm/ $^{\circ}\text{C}$) to distribute calibration pulses to all readout channels. The values of the calibration resistors in various parts of the detector are chosen to match the expected currents from particle showers [107, 109]. The calibration pulse is injected at the analogue input to the mother-board, which is the point closest to the origin of the analogue signals from the electrodes. Each presampler module is also equipped with a mother-board which collects signals from the readout cells and distributes the calibration pulses through a set of precision calibration resistors as mentioned above.

5.2.7 Quality-assurance tests

At each stage of the construction of the modules and assembly of the calorimeters, a number of quality-assurance tests were carried out. The most important tests were those performed after insertion of the calorimeters inside their cryostats and after the first cool-down and liquid-argon filling. All the signal and calibrations channels have been tested. Table 5.2 shows that the number of missing or bad channels is below the specified acceptable number of faults.

A high-voltage test at the nominal settings was also performed at this stage. After this first cold test, the calorimeters were heated back to room temperature before transportation and installation in the ATLAS pit. High-voltage tests have also been performed on all calorimeters in their final position in ATLAS. In the case of the barrel presampler and of the EMEC, most of the shorts can be eliminated by applying a high-voltage discharge [109, 111]. As a result, approximately 3% of the barrel electromagnetic channels and approximately 1% of the barrel and end-cap presampler and EMEC channels remain with shorts, and therefore will be powered at a reduced voltage, as explained in section 5.2.5.

5.3 Hadronic calorimeters

This section describes the ATLAS hadronic calorimeters: the tile calorimeter, the liquid-argon hadronic end-cap calorimeter (HEC) and the liquid-argon forward calorimeter (FCal).

5.3.1 Tile calorimeter

5.3.1.1 Overview

The tile calorimeter [105] is a sampling calorimeter using steel as the absorber and scintillator as the active medium. It is located in the region, $|\eta| < 1.7$, behind the liquid argon electromagnetic calorimeter and is subdivided into a central barrel, 5.8 m in length, and two extended barrels,

Table 5.2: Number of signal channels in each electromagnetic calorimeter layer and total number of calibration channels, pre-defined acceptable maximum rate and maximum number of faults, and numbers of faulty channels found after insertion at room temperature and later after cooling down and filling with liquid argon. Faulty channels correspond to either missing signal channels or signal channels with a bad signal shape [107, 109].

Layer	Number of channels	Maximum rate of faults accepted	Maximum number of faults accepted	Number of faulty channels	
				at room temperature	in liquid argon
Electromagnetic barrel calorimeter					
Presampler	7808	0.05%	4	0	0
Layer 1	57216	2 (per module)	64	9	11
Layer 2	28672	0.05%	14	2	5
Layer 3	13824	0.05%	6	0	4
Barrel end	2048	0.05%	1	3	3
Calibration	8192	0.05%	4	1	1
Electromagnetic end-cap calorimeter					
Presampler	1536	0.05%	1	0	1
Layer 1	28544	2 (per module)	32	3	4
Layer 2	23424	0.05%	12	2	7
Layer 3	10240	0.05%	5	0	2
Calibration	5952	0.05%	3	2	2

2.6 m in length and each having an inner radius of 2.28 m and an outer radius of 4.25 m, as shown in figure 1.3. The radial depth of the tile calorimeter is approximately 7.4λ (interaction lengths). Each barrel consists of 64 modules or wedges of size $\Delta\phi \sim 0.1$, made of steel plates and scintillating tiles [112].

The assembled module forms an almost-periodic steel-scintillator structure with a ratio by volume of approximately 4.7:1. The geometry is sketched in figure 5.9. The orientation of the scintillator tiles radially and normal to the beam line, in combination with wavelength-shifting fibre readout on the tile edges, allows for almost seamless azimuthal calorimeter coverage. The grouping of the readout fibres into the readout photomultiplier tubes (PMT's) provides an approximately projective geometry in pseudorapidity (see table 1.3). The gap region between the barrel and the extended barrel is instrumented with special modules, made of steel-scintillator sandwiches with the same sampling fraction as the rest of the tile calorimeter and with thin scintillator counters in the sectors where the available space in the gaps is even more limited. These devices allow to partially recover the energy lost in the crack regions of the detector and are described in more detail in section 5.5.

The electronics and readout of the tile calorimeter are highly integrated with the mechanical structure. The photomultiplier tubes and all the front-end electronics are mounted in 1.4 m long aluminium units, called drawers, which are inserted inside the support girder at the rear of each module (see section 5.6.1). The front-end electronics also provide analogue sums of subsets of the channels, forming trigger towers, for the L1 trigger (see section 5.6). The low-voltage power

supplies which power the readout are mounted in an external steel box, which has the cross-section of the support girder and which also contains the external connections for power and other services for the electronics (see section 5.6.3.1). Finally, the calorimeter is equipped with three calibration systems: charge injection, laser and a ^{137}Cs radioactive source. These systems test the optical and digitised signals at various stages and are used to set the PMT gains to a uniformity of $\pm 3\%$ (see section 5.6.2).

5.3.1.2 Mechanical structure

The mechanical structure of the tile calorimeter is designed as a self-supporting, segmented structure comprising 64 modules, each subtending 5.625 degrees in azimuth, for each of the three sections of the calorimeter [112]. The module sub-assembly is shown in figure 5.10. Each module contains a precision-machined strong-back steel girder, the edges of which are used to establish a module-to-module gap of 1.5 mm at the inner radius. To maximise the use of radial space, the girder provides both the volume in which the tile calorimeter readout electronics are contained and the flux return for the solenoid field. The readout fibres, suitably bundled, penetrate the edges of the girders through machined holes, into which plastic rings have been precisely mounted. These rings are matched to the position of photomultipliers. The fundamental element of the absorber structure consists of a 5 mm thick master plate, onto which 4 mm thick spacer plates are glued in a staggered fashion to form the pockets in which the scintillator tiles are located [113]. The master plate was fabricated by high-precision die stamping to obtain the dimensional tolerances required to meet the specification for the module-to-module gap. At the module edges, the spacer plates are aligned into recessed slots, in which the readout fibres run. Holes in the master and spacer plates allow the insertion of stainless-steel tubes for the radioactive source calibration system.

Each module is constructed by gluing the structures described above into sub-modules on a custom stacking fixture. These are then bolted onto the girder to form modules, with care being taken to ensure that the azimuthal alignment meets the specifications. The calorimeter is assembled by mounting and bolting modules to each other in sequence. Shims are inserted at the inner and outer radius load-bearing surfaces to control the overall geometry and yield a nominal module-to-module azimuthal gap of 1.5 mm and a radial envelope which is generally within 5 mm of the nominal one [112, 114].

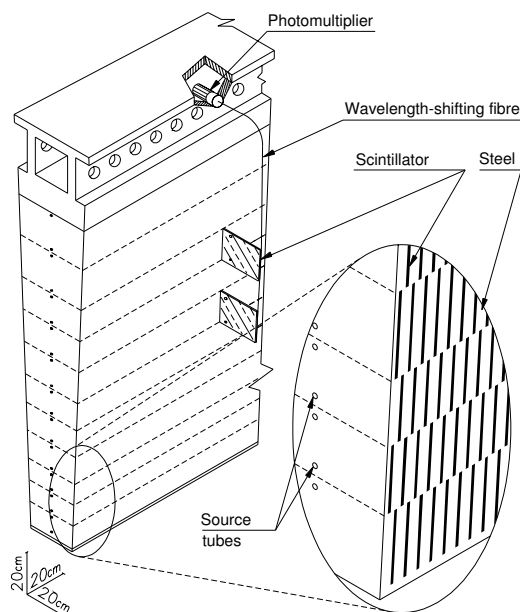


Figure 5.9: Schematic showing how the mechanical assembly and the optical readout of the tile calorimeter are integrated together. The various components of the optical readout, namely the tiles, the fibres and the photomultipliers, are shown.

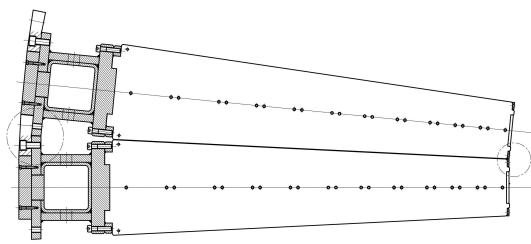


Figure 5.10: Azimuthal view of the tile-calorimeter module-to-module interface showing the bearing locations at the inner and outer radii, and the azimuthal gap with a nominal width at the inner radius of 1.5 mm, in which the readout fibres are routed to the photomultipliers inside the girder.

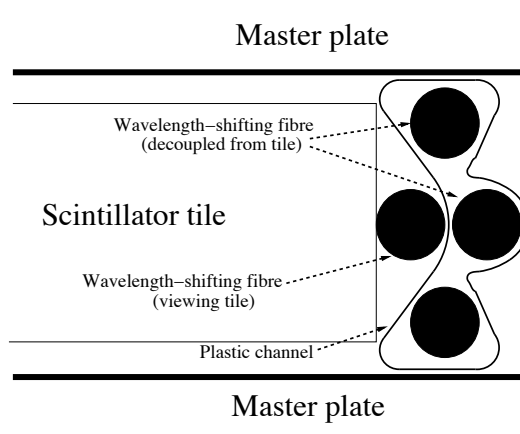


Figure 5.11: Radial view, looking inwards towards the interaction point, showing the fibre routing in the barrel modules. The fibre shown outside the channel accepts light for the tile onto which it is pressed. Further along the channel, this fibre is routed through a slot in the channel, into the interior region, while one of the other fibres is routed outside to view the next series of scintillator tiles in depth.

5.3.1.3 Optical components

Eleven sizes of scintillating tiles (one for each depth in radius) of 3 mm thickness and with radial lengths ranging from 97 mm to 187 mm and azimuthal lengths ranging from 200 mm to 400 mm form the active medium of the tile calorimeter. Ionising particles crossing the tiles induce the production of ultraviolet scintillation light in the base material (polystyrene) and this light is subsequently converted to visible light by wavelength-shifting fluors (the polystyrene is doped with 1.5% PTP as the primary fluor and with 0.044% POPOP as the secondary fluor). Over 460,000 scintillating tiles were produced for the tile calorimeter by injection molding of individual tiles: this eliminated the need for machining to form the trapezoidal shapes and drilling to cut the holes through which the calibration tubes must pass. The tolerance for all dimensions was held to ± 0.10 mm. Approximately 5% of the tile production was tested with a ^{90}Sr radioactive source and the results were used to characterise the light output of each small group of approximately twenty tiles in terms of maximum intensity and attenuation length [115]. Two sources of raw polystyrene were used for tile fabrication; during assembly, the groups of tiles were sorted so that tiles with similar response were inserted in contiguous areas of the detector.

Irradiation tests of tile/fibre assemblies indicated that in the first longitudinal sampling, for an integrated dose corresponding to ten years of operation at the LHC design luminosity, a light loss of less than 10% is expected. Smaller losses will occur in the other samplings, where the radiation dose is less.

Prior to insertion into the calorimeter, the tiles are inserted into a plastic sleeve, which both protects the tile and improves the scintillation light yield due to its high reflectivity of 95%. A mask pattern is printed on the sleeve to improve the optical uniformity. The resulting non-uniformity over the surface of a tile is generally below 5% for the sum of signals on both sides of the tile.

Wavelength-shifting fibres placed in contact with the tile edges collect the scintillation light produced in the scintillators and convert it to a longer wavelength. Each fibre collects light from tiles located at one or two radial depths in the calorimeter and transmits it to the PMT's located inside the girder. The fibres used have a diameter of 1 mm, are equipped with a double cladding and are characterised by an emission peak at 476 nm with a decay time of ~ 6 ns. As part of the quality control, light output and attenuation were measured for sample fibres from each of the 65 pre-forms used for fibre production. The fibres have an attenuation length of 325 cm at a wavelength of 430 nm, with a spread in attenuation length of $\sim 3\%$ and in light output of $\sim 3\%$ [116]. To improve the light output, the fibres are aluminised at the end opposite to the PMT. The aluminium mirrors were deposited using magnetron sputtering on bundles of 1261 fibres. The reflectivity was required to be 75% and the spread of its variation is $\sim 7\%$, based on measurements from a sample of fibres in each bundle [115]. The light output spread, at a fixed distance from the aluminised end, relative to a reference fibre, was found to be $\sim 3\%$ for each fibre length [117].

To facilitate assembly, a novel approach was developed to manage the 540,000 fibres required to read out the scintillator tiles and form calorimeter cells. The fibres (four for the central barrel and three for the extended barrel calorimeters) are inserted into a plastic channel much like a straw (see figures 5.9 and 5.11), which illustrate the scheme whereby depth segmentation is achieved in the readout. The channels are opaque to avoid light cross talk, and painted with a high-reflectivity ink on the side facing the tiles to maximise the light collection. Slots in the channels allow fibres to pass from a location in which they face a tile to a location in which they do not, in order to decouple the fibres at different depths in the calorimeter. The fibres were inserted in these channels using a robot [118] and are glued to the channel at a spot near the aluminised end of the fibre.

5.3.1.4 Instrumentation with scintillator and fibres

The light produced in the scintillating material is collected at the edges of each tile using two wavelength-shifting fibres as illustrated in figure 5.9. The fibres are grouped together and coupled to the PMT's which are housed at the outer edge of each module. The fibre grouping is used to define a three-dimensional cell structure in such a way as to form three radial sampling depths, approximately 1.5 , 4.1 and 1.8λ thick at $\eta = 0$. These cells have dimensions $\Delta\eta \times \Delta\phi = 0.1 \times 0.1$ in the first two layers and 0.2×0.1 in the last layer. The depth and η -segmentation of the barrel and extended barrel modules are shown in figure 5.12. The fibres coupled to each edge of the scintillating tiles are read out by two different PMT's to provide redundancy and sufficient information to partially equalise signals produced by particles entering the scintillating tiles at different impact positions.

Module instrumentation [119] comprised many steps, which ranged from cleaning the slots in the absorber structure to a set of final module quality-control measurements based on the individual tile fibre response. Following insertion of tiles and channel/fibre assemblies into a module, the fibres are grouped together to form cells and are glued as a bundle into the fibre-insertion tube, as

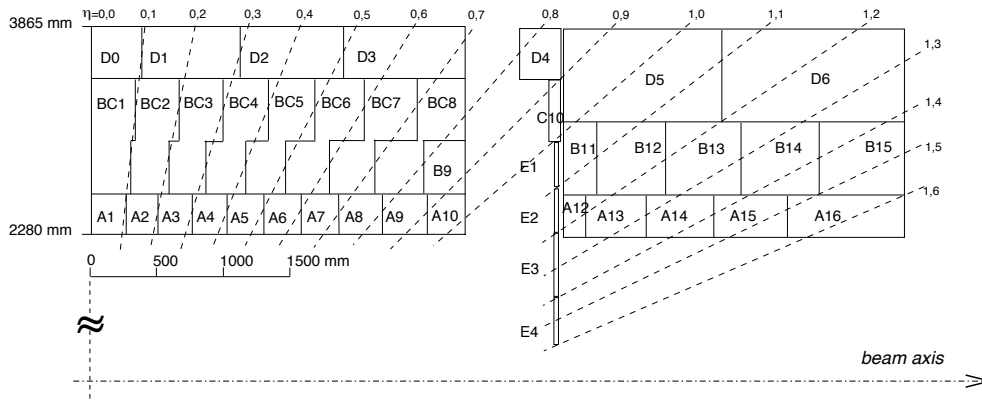


Figure 5.12: Segmentation in depth and η of the tile-calorimeter modules in the central (left) and extended (right) barrels. The bottom of the picture corresponds to the inner radius of the tile calorimeter. The tile calorimeter is symmetric about the interaction point at the origin.



Figure 5.13: Glued fibre bundle in girder insertion tube (left) and fibre routing (right) for tile-calorimeter module.

shown in figure 5.13. These tubes are then fixed into the girder plastic rings mentioned above, to obtain a precise match to the position of the photomultipliers. The tubes and fibres are then cut and polished inside the girder to give the optical interface to the PMT. This interface requires that these fibres be physically present at the time of module instrumentation. However, the gap and crack scintillators described in section 5.5 are mounted only following calorimeter assembly in the cavern. An optical connector is used, therefore, to couple the light from their readout fibres to the already glued and polished optical fibres which penetrate the girder.

Quality-control checks have been made at several moments during the instrumentation process: during fibre bundling and routing, during fibre gluing, cutting and polishing, during tile-fibre optical coupling when the tile was excited by either a blue LED or a ^{137}Cs γ -source. Tile-fibre pairs with a response below 75% of the average response of the tile row for the cell under consideration were repaired in most cases (typically by re-insertion of the plastic channel to improve tile-fibre

optical coupling or replacement of the fibre). The average cell response uniformity for production modules, measured using the caesium source, is shown in figure 5.14 and meets the design specification of 10%.

5.3.2 Hadronic end-cap calorimeters (HEC)

5.3.2.1 Overview

Figure 5.15 shows a schematic view of the design of a HEC module. The hadronic end-cap calorimeter (HEC) [104, 120] is a copper/liquid-argon sampling calorimeter with a flat-plate design, which covers the range $1.5 < |\eta| < 3.2$. The HEC shares each of the two liquid-argon end-cap cryostats with the electromagnetic end-cap (EMEC) and forward (FCal) calorimeters (see figure 5.25). The HEC consists of two wheels in each end-cap cryostat: a front wheel (HEC1) and a rear wheel (HEC2), each wheel containing two longitudinal sections. The wheels are cylindrical with an outer radius of 2030 mm. Each of the four HEC wheels is constructed of 32 identical wedge-shaped modules, as illustrated in figure 5.16. A stainless-steel connecting-bar system at the outer wheel perimeter guarantees the mechanical integrity of the wheel structure. At the inner radius, small copper connecting bars link the plates of each set of neighbouring modules. Two sliding rails support the wheels inside the cryostat and are an integral part of the mechanical structure. The final vertical deformation of the wheel structure has been measured for the four wheels to represent a sag of 0.3 mm on average. The wheels remain perpendicular to their axis within ± 1.0 mm.

The modules of the front wheels are made of 24 copper plates, each 25 mm thick, plus a 12.5 mm thick front plate. In the rear wheels, the sampling fraction is coarser with modules made of 16 copper plates, each 50 mm thick, plus a 25 mm thick front plate. The gaps in between the plates all have a thickness of 8.5 mm. The resulting sampling fractions for HEC1 and for HEC2 are 4.4% and 2.2% respectively. The wheels have an inner radius of 372 mm for the first nine plates of HEC1 and of 475 mm for the remaining plates of HEC1 and for all 17 plates of HEC2. The structural strength of the modules is provided by seven stainless-steel tie-rods with 12 mm (16 mm) diameter for the front (rear) modules. Annular high-precision spacers on the tie-rods maintain the 8.5 mm gaps between the copper plates.

Three electrodes divide the 8.5 mm gaps into four separate LAr drift zones of 1.8 mm width each. Figure 5.17 shows schematically the arrangement of the readout structure. The space between the electrodes is maintained using a honeycomb sheet which is also held in place by the seven

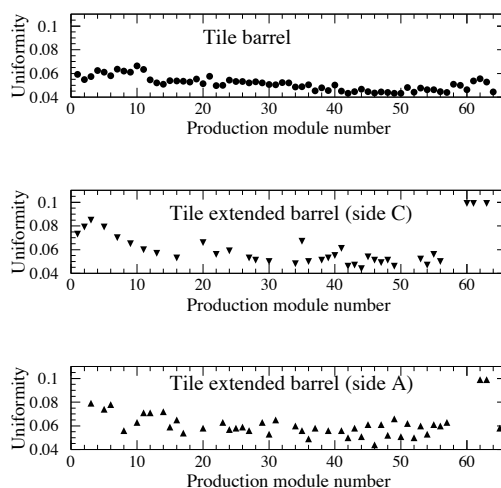


Figure 5.14: Average cell response uniformity, measured using the caesium calibration system for the barrel and the two extended barrel tile calorimeters.

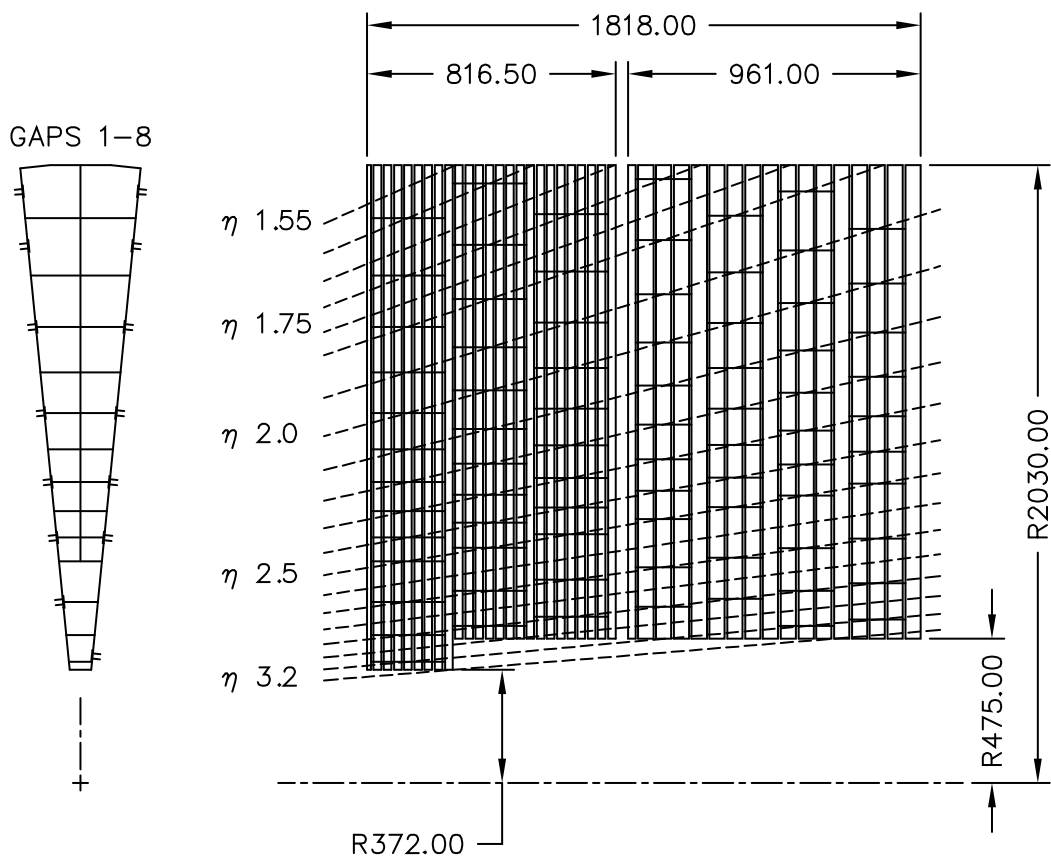


Figure 5.15: Schematic $R - \phi$ (left) and $R - z$ (right) views of the hadronic end-cap calorimeter. The semi-pointing layout of the readout electrodes is indicated by the dashed lines. Dimensions are in mm.

tie-rods. Each drift zone is individually supplied with high voltage (see table 5.1). The middle electrode carries a pad structure covered by a high-resistivity layer, serving as the readout electrode and defining the lateral segmentation of the calorimeter. The two other electrodes carry surfaces of high resistivity to which high voltage is applied. These high-voltage planes form an electrostatic transformer (EST). Electrically, this structure corresponds to a double gap of 3.6 mm each. The EST structure has the advantage of a lower high-voltage for operation, of a double high-voltage safety and thus of reduced problems with space-charge effects due to ion density at large values of $|\eta|$. For the nominal high voltage of 1800 V, the typical drift time for electrons in the drift zone is 430 ns.

The readout cells are defined by pads etched on the central foil in each gap. The arrangement of these pads provides a semi-pointing geometry (see figure 5.15). The size of the readout cells is $\Delta\eta \times \Delta\phi = 0.1 \times 0.1$ in the region $|\eta| < 2.5$ and 0.2×0.2 for larger values of η .

The signals from the pads of this electrode structure are amplified and summed employing the concept of active pads [121]: the signals from two consecutive pads are fed into a separate preamplifier (based on GaAs electronics). The use of GaAs preamplifiers in the cold provides the

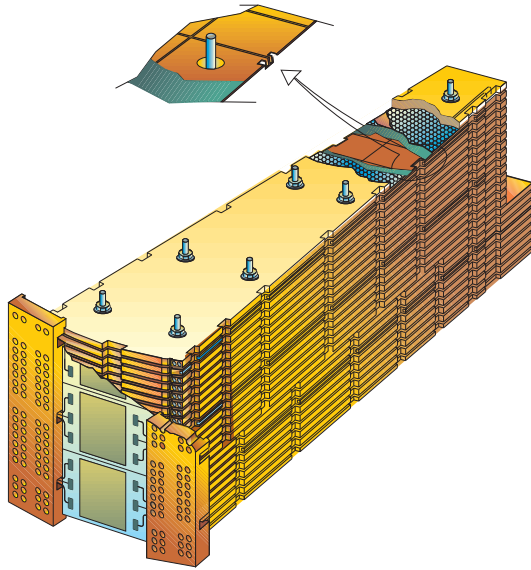


Figure 5.16: Schematic view of a HEC module, with a cut-away showing the readout structure and the active-pad electronics.

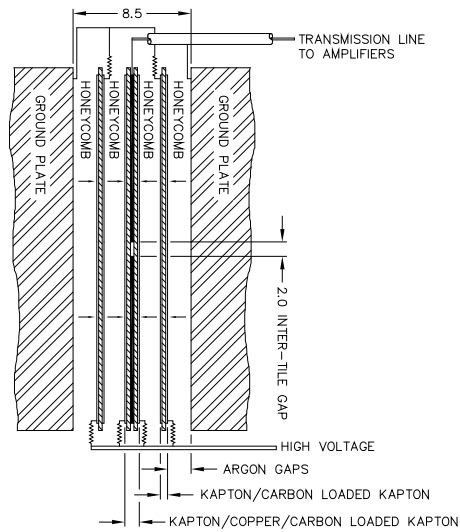


Figure 5.17: Schematic of the arrangement of the HEC readout structure in the 8.5 mm inter-plate gap. All dimensions are in mm.

optimum signal-to-noise ratio for the HEC. An important aspect of the HEC is its ability to detect muons and to measure any radiative energy loss. The density of the electronics on the HEC wheels with their rather modest number of read-out channels (5632 in total) and the power consumption of the GaAs integrated circuits (15 mW for one preamplifier channel and approximately 200 mW for the entire chip) are sufficiently low that the heating effect of the electronics on the liquid argon does not produce bubbling. The outputs of the preamplifiers are summed on the same GaAs integrated circuit to produce one signal from each cell. The signal sent to the feed-through for each cell is thus comprised of the amplified and summed signals of the eight or sixteen pads with the same η and ϕ within a readout section.

5.3.2.2 Wheel assembly and installation

Figure 5.18 shows a HEC wheel fully assembled on its assembly table. The geometrical precision of the wheel is given by 32 datum pins on the assembly table. During the wheel assembly, each module had to pass a series of quality-assurance tests: high-voltage reliability, capacitance control, electronic cabling and signal reconstruction verification using the calibration procedures in warm and in cold. These tests were repeated after the wheel assembly, after the wheel rotation, after the wheel insertion, after the full cabling of the HEC1 and HEC2 wheels inside the cryostat and finally through the feed-throughs of the cryostat.

After closing the end-cap cryostat, each end-cap has been cooled down, filled with LAr and the final cold tests prior to the movement to the ATLAS cavern have been performed. For the HEC,

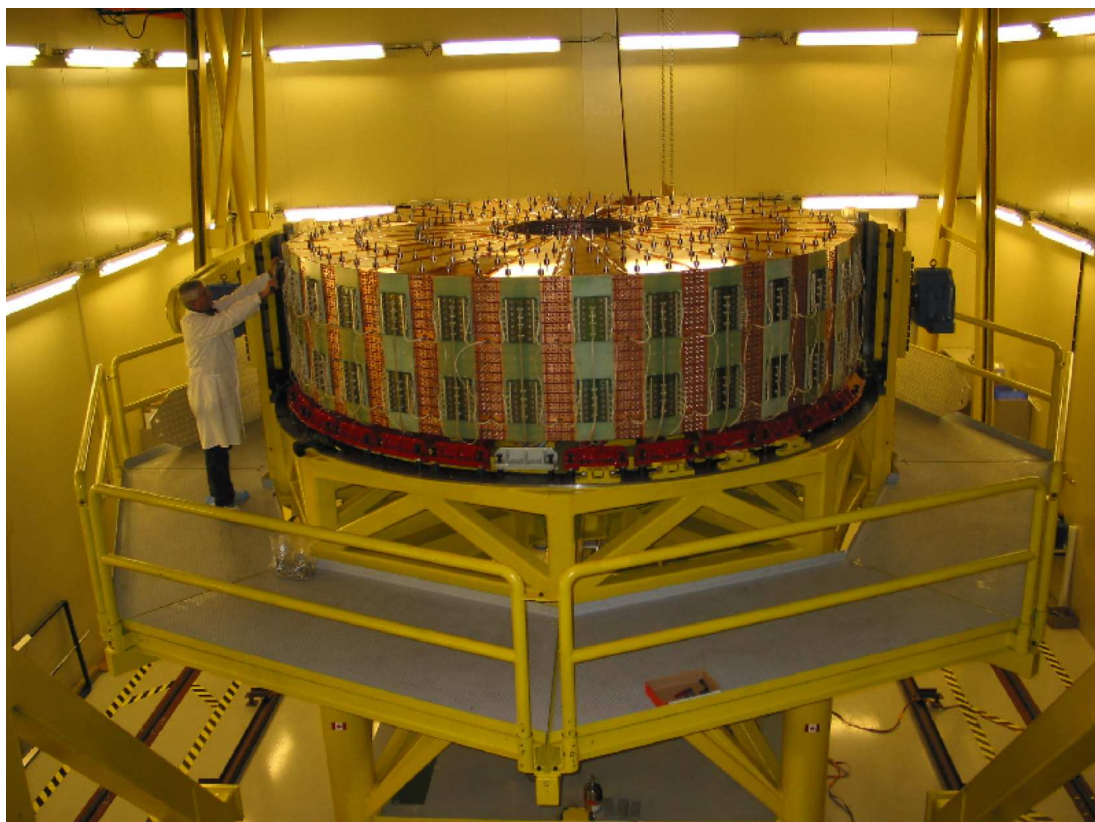


Figure 5.18: Photograph of a fully assembled HEC wheel on the assembly table. The active-pad electronic boards located on the outer circumference are clearly visible.

these tests included quality-assurance measurements and cabling checks of all signal and calibration lines, full calibration and delay scans of all signal channels, full pulse-shape analysis of all signal channels, detailed noise measurements of all channels including coherent noise and a long-term high-voltage test of all high-voltage lines. Typically, three signal channels per end-cap were found to be not fully operational, corresponding to 0.1 % of all channels, as shown in table 5.3. The fraction of high-voltage lines with shorts was $\sim 4\%$ in liquid argon, but, most importantly, with four individual high-voltage lines per individual HEC gap, all HEC regions are operational (see also table 5.1 which lists the nominal high-voltage settings for the HEC).

5.3.3 Forward calorimeters

5.3.3.1 Overview

The forward calorimeters (FCal) are located in the same cryostats as the end-cap calorimeters and provide coverage over $3.1 < |\eta| < 4.9$. The close vicinity and coupling between these systems result in a quite hermetic design, which minimises energy losses in cracks between the calorimeter systems and also limits the backgrounds which reach the muon system. As the FCal modules are located at high η , at a distance of approximately 4.7 m from the interaction point, they are exposed

Table 5.3: Table showing the number of faulty signal channels in each segment and the number of faulty calibration lines for both hadronic end-caps after insertion at room temperature and afterwards in liquid argon.

HEC module and section	Total number of channels	Number of faulty channels (ambient)	Number of faulty channels (in liquid)	Percentage (%)
HEC1 (first section)	1536	0	0	0
HEC1 (second section)	1472	0	3	0.20
HEC2 (first section)	1344	0	0	0
HEC2 (second section)	1280	1	2	0.16
Calibration	1024	1	1	0.1

Table 5.4: Table of parameters for the three FCal modules.

	FCal1	FCal2	FCal3
Function	Electromagnetic	Hadronic	Hadronic
Mass of module (kg)	2119	3826	3695
Main absorber material	Copper	Tungsten	Tungsten
LAr gap width (mm)	0.269	0.376	0.508
Radiation length (X_0)	27.6	91.3	89.2
Absorption length (λ)	2.66	3.68	3.60
Number of electrodes	12260	10200	8224
Number of readout channels	1008	500	254

to high particle fluxes. This has resulted in a design with very small liquid-argon gaps, which have been obtained by using an electrode structure of small-diameter rods, centred in tubes which are oriented parallel to the beam direction. The liquid-argon gaps are smaller than the usual 2 mm gap of the electromagnetic barrel calorimeter to avoid ion build-up problems and to provide at the same time the highest possible density. These smaller gaps also lead to a faster signal with roughly the same instantaneous current but smaller integrated current. In the electromagnetic layer (FCal1), the triangular current pulse at the electrode has a full drift time of 60 ns. For FCal2 and FCal3, the full drift time scales with the gap size since the field in the gaps is similar for all three modules.

5.3.3.2 Module description

Each FCal is split into three 45 cm deep modules: one electromagnetic module (FCal1) and two hadronic modules (FCal2 and FCal3), as illustrated in figure 5.19. To optimise the resolution and the heat removal, copper was chosen as the absorber for FCal1, while mainly tungsten was used in FCal2 and FCal3, to provide containment and minimise the lateral spread of hadronic showers. A shielding plug made of a copper alloy has been mounted behind FCal3 to reduce backgrounds in the end-cap muon system. A full description of the FCal detector can be found in [122].

The basic parameters of the FCal modules are listed in table 5.4. The FCal1 layer is made of copper plates stacked one behind the other. The plates have 12,260 holes drilled in them through which the electrode structures are inserted. An electrode consists of a co-axial copper rod and

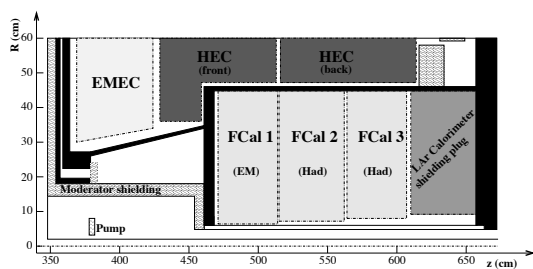


Figure 5.19: Schematic diagram showing the three FCal modules located in the end-cap cryostat. The material in front of the FCal and the shielding plug behind it are also shown. The black regions are structural parts of the cryostat. The diagram has a larger vertical scale for clarity.

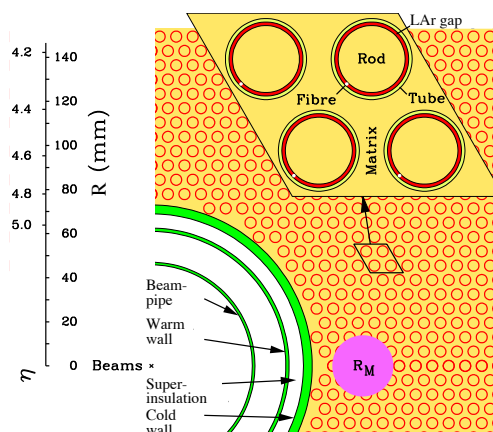


Figure 5.20: Electrode structure of FCal1 with the matrix of copper plates and the copper tubes and rods with the LAr gap for the electrodes. The Molière radius, R_M , is represented by the solid disk.

copper tube separated by a precision, radiation-hard plastic fibre wound around the rod. The arrangement of electrodes and the effective Molière radius for the modules can be seen in figure 5.20. Mechanical integrity is achieved by a set of four tie-rods which are bolted through the structure. The electrode tubes are swaged at the signal end to provide a good electrical contact.

The hadronic modules FCal2 and FCal3 are optimised for a high absorption length. This is achieved by maximising the amount of tungsten in the modules. These modules consist of two copper end-plates, each 2.35 cm thick, which are spanned by electrode structures, similar to the ones used in FCal1, except for the use of tungsten rods instead of copper rods. Swaging of the copper tubes to the end-plates is used to provide rigidity for the overall structure and good electrical contact. The space between the end-plates and the tubes is filled with small tungsten slugs, as shown in figure 5.21. The inner and outer radii of the absorber structure formed by the rods, tubes and slugs are enclosed in copper shells.

Signals are read out from the side of FCal1 nearer to the interaction point and from the sides of FCal2 and FCal3 farther from the interaction point. This arrangement keeps the cables and connectors away from the region of maximum radiation damage which is near the back of FCal1. Readout electrodes are hard-wired together with small interconnect boards on the faces of the modules in groups of four, six and nine for FCal1, FCal2 and FCal3 respectively. The signals are then routed using miniature polyimide co-axial cables along the periphery of the FCal modules to summing boards which are mounted on the back of the HEC calorimeter. The summing boards are equipped with transmission-line transformers which sum four inputs. High voltage (see table 5.1) is also distributed on the summing boards via a set of current-limiting resistors, as shown in figure 5.22 for the specific case of FCal1. The signal summings at the inner and outer radii of the modules are in general different due to geometric constraints and higher counting rates at the inner radius [122].

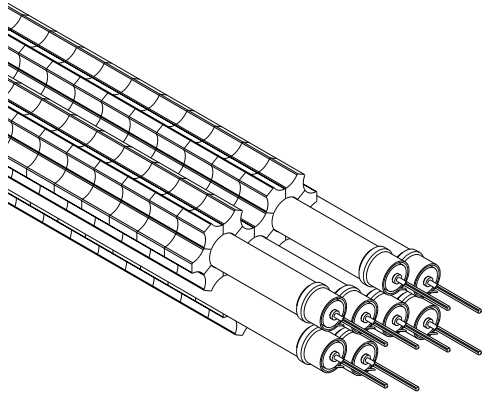


Figure 5.21: View of the FCal hadronic module absorber matrix, including a set of tungsten rods and copper tubes surrounded by 1 cm long tungsten slugs.

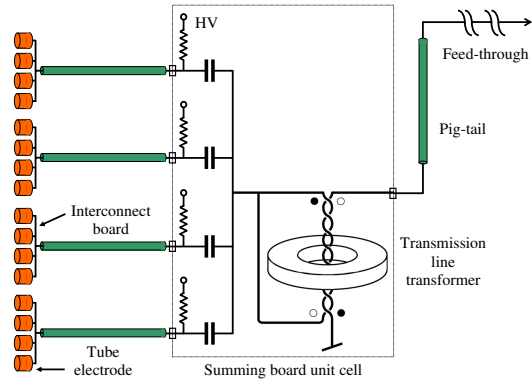


Figure 5.22: Schematic of the FCal1 module cabling from the electrodes to the cryogenic feed-through. The other modules differ only by the number of rods grouped together on the interconnect board (six for FCal2 and nine for FCal3).

5.3.3.3 Integration into the cryostat

There are two sets of FCal modules, one on each side of the interaction point. Each set of modules, along with a shielding plug, are mounted inside a cylindrical tube, known as the FCal support tube, which is shown as the black horizontal line between the FCal and the HEC in figure 5.19. This support tube, along with an upstream conical nose and a downstream flange are the structural components at the inner radius of the end-cap cryostat. To load the modules into the support tube, a mandrel was used as a temporary support for the modules. This stage of the assembly is illustrated in figure 5.23. This arrangement allowed the readout cables to be dressed in the cable trays along the sides of the modules. The support tube was then slid over the modules, the module weights were transferred to the support tube and the cone and flange were attached to the support tube, as shown in figure 5.24. The complete unit was then installed into the end-cap cryostat. At this point, the cables were connected to the FCal summing boards.

5.3.3.4 Placement of FCal

There is only a small clearance between the FCal modules and the FCal support tube, such that the $x - y$ position of each module is fixed relative to the tube. The central axis of the detectors is about 1 mm below the central axis of the support tube. The distance between modules is constrained by bumpers attached to the end-plates of the modules. In this manner, the modules can move in the z direction within the tubes, but will be within approximately 1 mm of their design location. The survey of the FCal is then a matter of a survey of the FCal support tube. This was carried out after the installation of the FCal into the cryostat. The central axis of the support tube is within about 2 mm of the central axis of the cryostat outer warm vessel and has been surveyed to a precision of about 0.3 mm.



Figure 5.23: Assembly of FCal modules: from left to right, the three modules plus the copper alloy plug can be seen on the support mandrel with most of the cabling in place.



Figure 5.24: Completed FCal assembly with its bulkhead and cone attached, just before insertion into the end-cap cryostat.

5.3.3.5 Tests during installation/integration

A series of quality-control checks were carried out on the modules. These included high-voltage testing, capacitance measurements and reflection testing. The results of the capacitance measurements provided a measure of the uniformity of the electrodes. High-voltage checks were carried out at each stage of assembly and integration of the detectors both at warm and at cold. It was found that the number of shorts did vary during this process. The reflection tests were used to look for other detector faults, such as disconnected channels and broken ground braids.

A summary of the faults observed in the FCal modules after the cryostats were installed in the ATLAS cavern and filled with liquid argon can be found in table 5.5. The right-hand column shows the number of readout channels per module which have a fault leading to a distorted signal, a reduction in signal amplitude or to both of these effects. It is expected that the output from these channels can be adjusted in the signal reconstruction to partially recover the true amplitude, including when the fault arises from high-voltage problems. The 1762 channels in each FCal are served by 112 high-voltage lines. Two of these were lost during the FCal integration into the end-cap cryostat, one for FCal1 on side C and the other for FCal3 on side A. This accounts for the large number of faulty channels shown for these two modules in table 5.5. There are sixteen high-voltage shorts on the FCal on side A and nine on side C. These account for roughly half of the remaining faults listed in table 5.5. The other half are dominated by damaged blocking capacitors (see figure 5.22). A more detailed description of the faults observed in the modules can be found in ref. [122].

Table 5.5: Summary of faults found in the FCal modules after installation in ATLAS. Shown for each module are the total number of channels, the number of dead channels and the number of faulty channels which will require special treatment in the reconstruction of the signal (see text). Faulty channels correspond to either missing signal channels or signal channels with a bad signal shape [122].

Module	Channels		
	Total number of channels	Number of dead channels	Number of faulty channels
FCal1 (side A)	1008	0	26
FCal2 (side A)	500	1	4
FCal3 (side A)	254	1	59
FCal1 (side C)	1008	5	51
FCal2 (side C)	500	0	8
FCal3 (side C)	254	1	4

5.4 Cryostats and associated feed-throughs

5.4.1 Cryostat description

As mentioned above, the liquid-argon calorimeters are located in three different cryostats. Figure 1.3 shows the general features and location of the barrel and end-cap cryostats in the overall calorimeter system. Each cryostat is composed of two concentric aluminium vessels, an inner cold vessel and an outer warm vessel. Each vessel forms a cylindrical torus centred on the beam axis and the space in between the vessels is under vacuum. As described in section 2.1.1, the central solenoid is housed in the insulating vacuum of the barrel cryostat and supported by the inner cylinder of the warm barrel vessel. The two end-cap cryostats each house one electromagnetic end-cap calorimeter (EMEC), one hadronic end-cap calorimeter (HEC) and one forward calorimeter (FCal). Figure 5.25 shows a more detailed cut-away view of one end-cap cryostat with the three different calorimeter systems it contains.

The different vessels are closed at both ends by bulkheads. All bulkheads are circular-shaped plates with passage holes. The barrel passage holes allow the insertion of the inner detector and of its associated beam-pipe into the inner warm vessel bore. The end-cap passage holes allow the passage of the next section of the beam-pipe and the insertion of its associated pump station (see section 9.8). The barrel bulkheads and the inner cold vessel of the barrel cryostat have tapered walls to minimise the material and dead space between the interaction region and the electromagnetic calorimeters. To further minimise the amount of material, the cold and warm front end-cap bulkheads are flat, and insulating spacers allow the warm bulkhead to sit on the cold one.

The cold vessels rest on four feet made of a glass-fibre composite material, which provide electrical and thermal insulation to the warm vessels. The barrel cryostat load is transferred directly to the ATLAS main rail system through the tile-calorimeter support saddles. For the support on

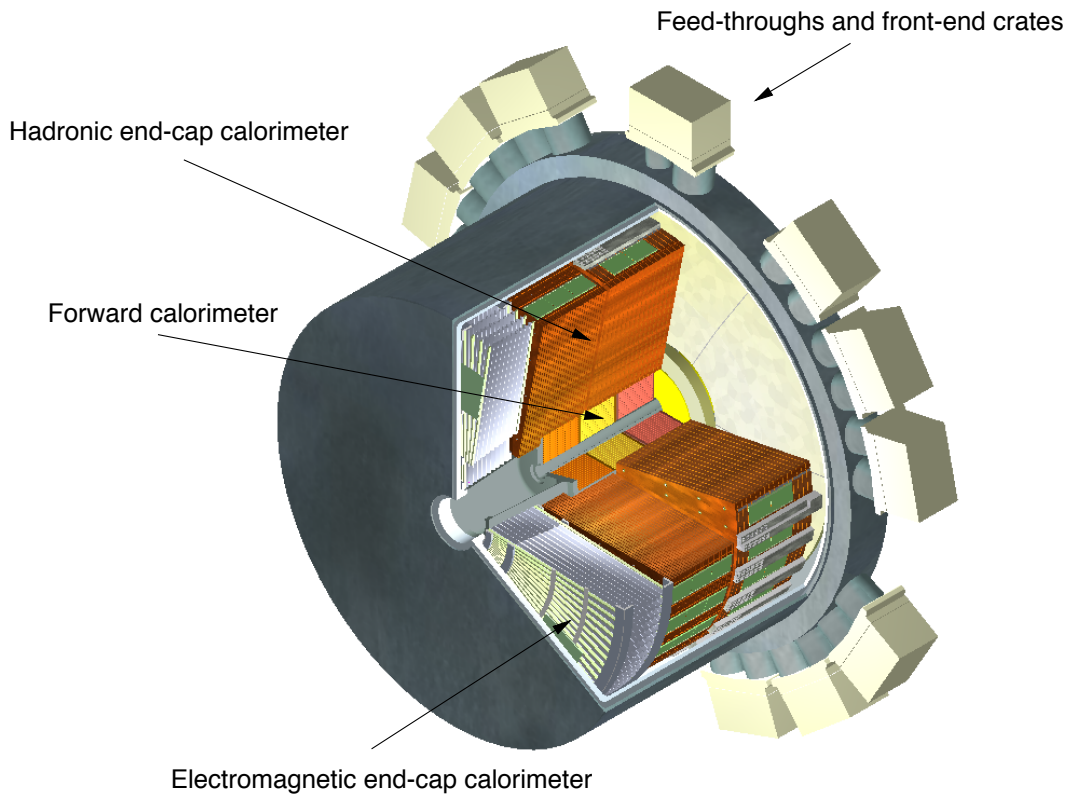


Figure 5.25: Cut-away view of an end-cap cryostat showing the positions of the three end-cap calorimeters. The outer radius of the cylindrical cryostat vessel is 2.25 m and the length of the cryostat is 3.17 m.

the side of the end-cap cryostat pointing towards the interaction point, this is not possible and the load is transferred through the inner radius of the extended calorimeter on a vertically adjustable support.

5.4.2 Signal feed-throughs

The signal feed-throughs bring all the signal, monitoring, calibration and spare lines through the insulating vacuum from the liquid-argon cold volume to the front-end crates located at room temperature around and on the outside of the barrel and end-cap cryostats. A total of 64 feed-throughs serve the 122,800 lines of the barrel electromagnetic calorimeter, whereas a total of 2×25 feed-throughs serve the $2 \times 48,000$ lines of the two end-caps. In each end-cap, 20 feed-throughs are used by the EMEC, four by the HEC and one by the FCal (the EMEC uses also part of the four HEC feed-throughs).

A feed-through [123] consists primarily of a warm flange and a cold flange, with a flexible bellows welded between them. The volume between the two flanges is under vacuum. Each flange houses four gold-plated pin carriers, providing a total of 1920 signal connections per feed-through.

Both pin carriers are interconnected with flat polyimide strip-line flexible cables. To minimise the lengths of the connection lines, the signal feed-throughs are distributed radially around each end of the barrel cryostat and at the back of each of the end-cap cryostats.

5.4.3 High-voltage feed-throughs

Two high-voltage feed-through ports [124] are mounted on each cryostat. They are located close to the highest point at each end of the barrel cryostat and at the back of each end-cap cryostat. A port consists of a single warm bulkhead mounted on the warm vessel, from which the wire bundle leads to the calorimeter via a tube connected to the cold vessel by stainless-steel bellows. The liquid argon rises up to the bellows and is followed, instead of vacuum, by a 70 cm high column of argon gas at 1.25 bar. With such an arrangement, the HV wires are never under vacuum and thus not subject to corona effects. The high-voltage wire consists of a solid 0.41 mm diameter constantan (Cu/Ni alloy) conductor with a 0.30 mm thick radiation-hard plastic (polyether-etherketone) cladding. Each port holds approximately 840 HV lines. These lines serve the standard high-voltage lines and the spares may be used to supply single electrodes or split sectors which do not hold the nominal high voltage (see section 5.2.5).

5.5 Instrumentation in gap between cryostats

The transition region or gap between the barrel and end-cap calorimeters is filled with cables and services for the inner detector as well as power supplies and services for the barrel liquid-argon calorimeter. One of the standard gap regions is shown in figures 5.12 and 5.26. At the outer radius of the detector, a reduced section of a standard tile-calorimeter sub-module, the plug, provides additional coverage in this region and significantly reduces the neutron flux from the inner-detector volume into the muon system.

In the region of the tile-calorimeter module where part of the calorimeter structure has been removed, two scintillators (E1 and E2 shown in figure 5.12) with independent readout (the gap scintillators) are attached to the module surface. The gap scintillators cover the region $1.0 < |\eta| < 1.2$ and provide signals which can be used to correct for energy losses in the inactive material in the gap.

Two scintillators (E3 and E4 shown in figure 5.12), the cryostat scintillators, penetrate the region between the outer walls of the barrel and end-cap cryostats. These are physically attached to the tile calorimeter and read out through its electronics. The cryostat scintillators cover the region $1.2 < |\eta| < 1.6$ and provide a signal which can be used to correct for energy losses in the outer wall of the barrel cryostat and in the inner-detector services. Both gap and crack scintillators have full coverage in ϕ , with a segmentation of $\Delta\phi = 0.1$.

For initial data-taking at low luminosities, two sets of sixteen scintillator counters installed on the front face of the end-cap calorimeter cryostats will be used to trigger on minimum-bias events. Each set of counters is segmented in eight units in ϕ and two units in η . They are located at $|z| = 3560$ mm, the innermost set covers radii between 153 mm and 426 mm, corresponding to the region $2.82 < |\eta| < 3.84$ and the outermost set covers radii between 426 mm and 890 mm, corresponding to the region $2.09 < |\eta| < 2.82$. The readout for these counters will be provided by that of sixteen of the cryostat scintillators covering the region $1.2 < |\eta| < 1.4$. Eight of

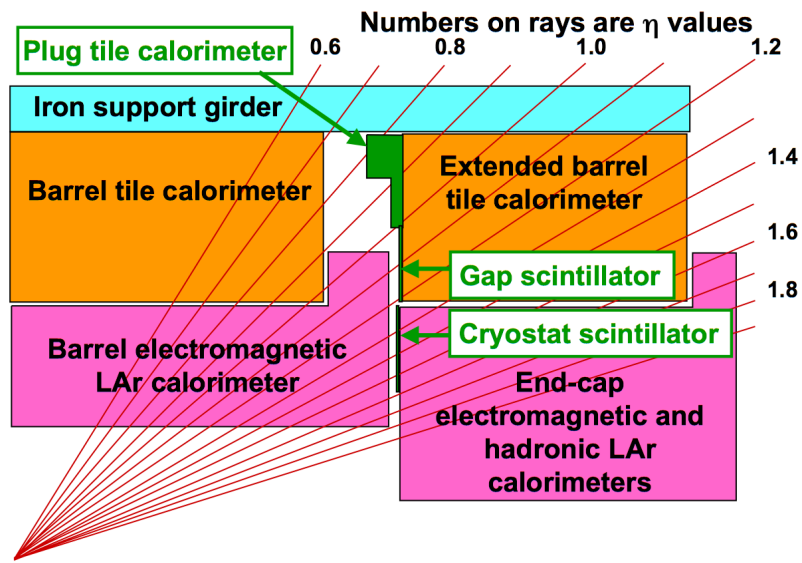


Figure 5.26: Schematic of the transition region between the barrel and end-cap cryostats, where additional scintillator elements are installed to provide corrections for energy lost in inactive material (not shown), such as the liquid-argon cryostats and the inner-detector services. The plug tile calorimeter is fully integrated into the extended barrel tile calorimeter. The gap and cryostat scintillators are read out together with the other tile-calorimeter channels (see text).

these cryostat scintillators had to be removed on each side for the routing of the signals from the minimum-bias scintillators. They will be reinserted for operations at full luminosity.

There are several locations around the circumference of the calorimeter, in which the standard gap instrumentation is not possible, for example the region opposite the support feet for the barrel cryostat [112]. In these locations, the plug calorimeter is reduced further in its length. In the location of the exit of the barrel cryogenic line, no plug calorimeter can be accommodated and it is replaced entirely by scintillators. Finally, the inner support of the end-cap cryostat sits on the tile calorimeter at its inner radius. In these regions, the tile-calorimeter modules themselves are cut to provide the support surface on which the cryostat support jacks sit. The gap scintillators are also missing in this region.

5.6 Calorimeter readout electronics, calibration and services

5.6.1 Readout electronics

5.6.1.1 Overview

This section describes the on-detector (front-end) and off-detector (back-end) electronics of the ATLAS calorimetry. The major tasks required of the readout electronics are to provide the first-level (L1) trigger system with the energy deposited in trigger towers of size $\Delta\eta \times \Delta\phi = 0.1 \times 0.1$ and to measure, for L1-triggered beam crossings, the energy deposit in each calorimeter cell to the

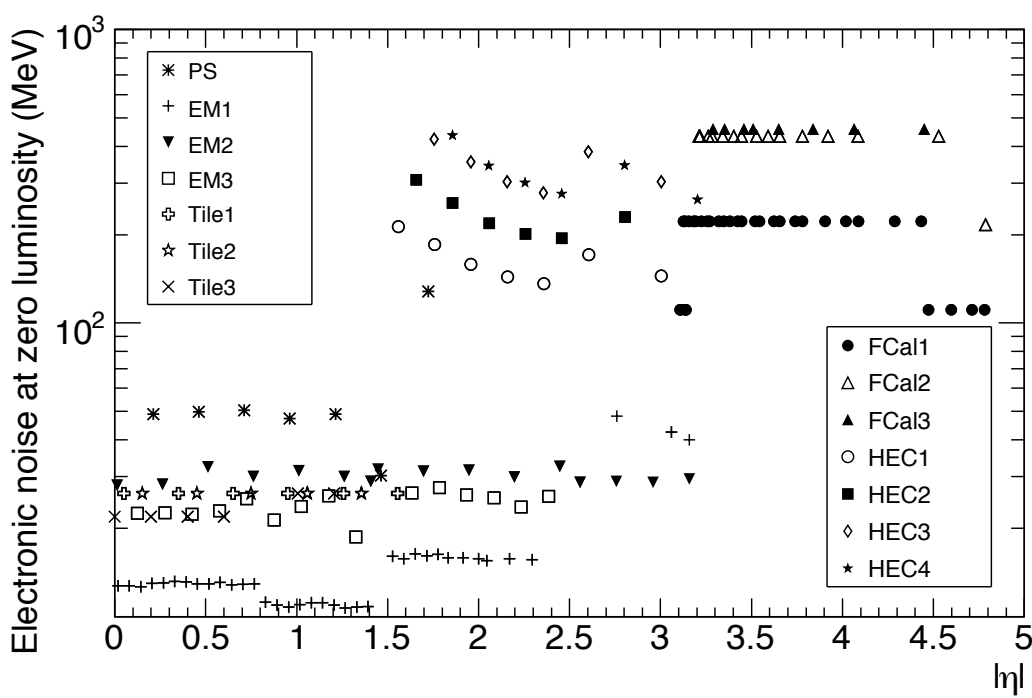


Figure 5.27: Expected electronic noise in individual cells of the various sampling layers of the calorimeters as a function of $|\eta|$. Note that the presampler noise is corrected for by the appropriate sampling fractions as discussed in section 5.6.2.1.

specifications set by the performance requirements. The dynamic range to be covered ranges from a maximum of 3 TeV down to a lower limit of ~ 10 MeV set by thermal noise in the calorimeters. The thermal noise from the front-end electronics varies widely across the various calorimeter systems, as illustrated in figure 5.27. Coherent noise over the many cells used to measure electron/photon energies in the electromagnetic calorimeters and jet energies and E_T^{miss} in the overall calorimetry should be kept below 5% of the incoherent noise. The readout should proceed without any appreciable dead-time up to a trigger rate of 75 kHz.

As already described for the overall experiment in section 3.1, all electronics components situated in the cavern have to be radiation-tolerant to specifications including large safety factors. However, the necessity for a large dynamic range and for very low coherent noise favours a readout architecture with analogue processing very close to the detectors. These quite stringent requirements have led to solutions where the analogue signals are amplified, processed and digitised by radiation-tolerant front-end electronics mounted very near the detectors (just above the signal feed-throughs for the LAr calorimeters and in drawers incorporated into the girders for the tile calorimeters) and followed by subsequent digital processing of the signals in back-end systems which are located off-detector. For example, the overall readout architecture of the LAr calorimeters is sketched out in figure 5.28. This overall electronics readout system [125, 126] is used for all the LAr calorimeters and, as shown in figure 5.28, provides also the necessary input for the L1 calorimeter trigger (see section 8.2).

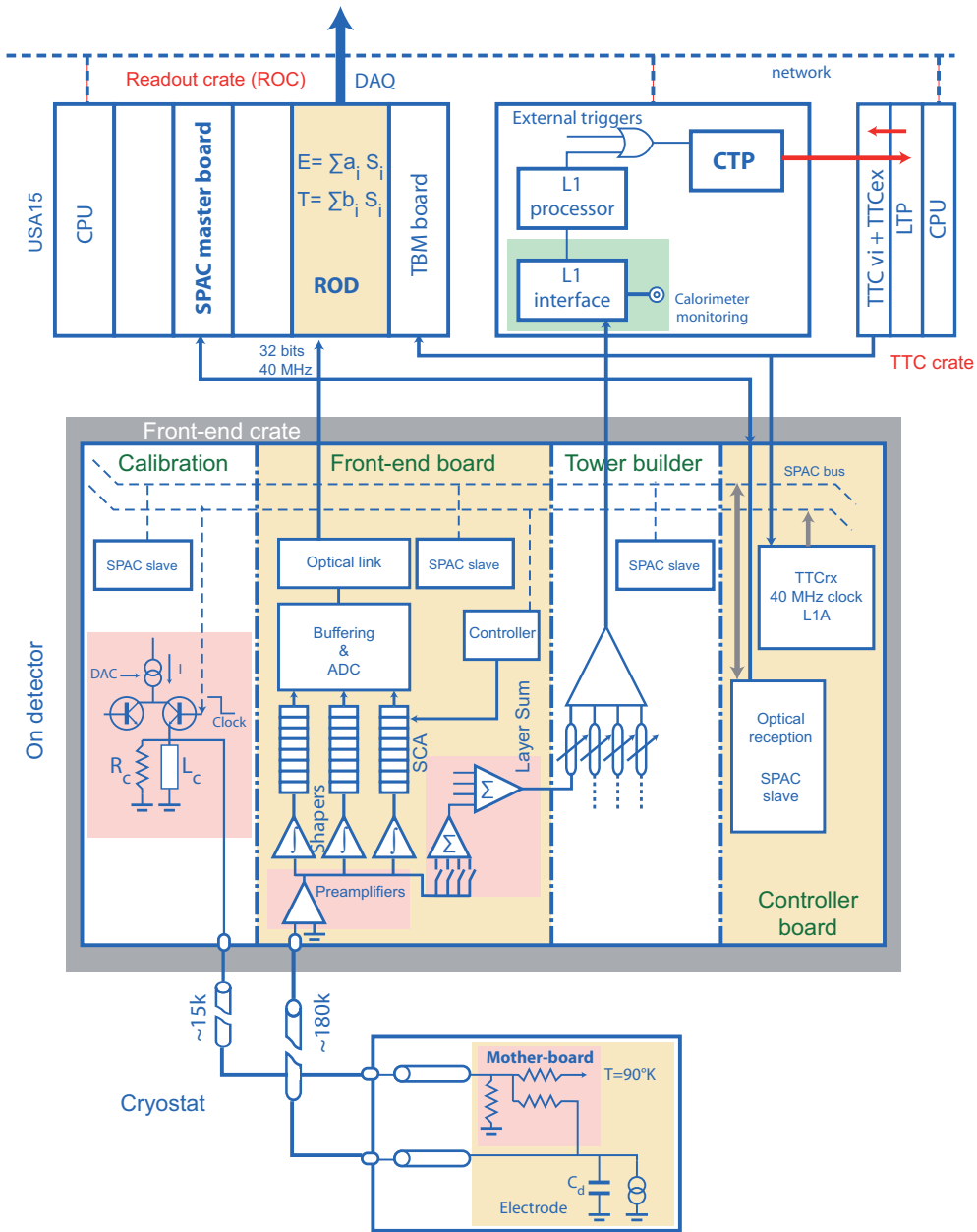


Figure 5.28: Block diagram depicting the architecture of the overall LAr readout electronics. The lower box depicts the cold electrical circuit in the calorimeter cryostat. The central box illustrates the functionality of the front-end boards located in the on-detector front-end electronics crates which are mounted on the cryostat feed-throughs. The upper layer shows the off-detector back-end electronics components (ROD boards and TTC modules) mounted in their readout crates, together with the LAr front-end tower builder electronics and the interfaces to the L1 trigger system with its central trigger processor (CTP).

The radiation levels in the vicinity of the LAr cryostats and tile drawers (fluences of 10^{12} neutrons per cm^2 per year and ionising doses of 20 Gy per year) have required the development and use of a large number of specifically designed radiation-hard ASIC's for many key components of the front-end electronics of the calorimeters. The back-end systems, located in the main services cavern (USA15), where there are no radiation issues, use commercial components. The back-end electronics systems for all LAr calorimeters and for the tile calorimeter have been designed with the same architecture, although some important differences exist in the functional implementation.

As discussed in section 9.4.8, an important effort has been invested in implementing the grounding and electromagnetic compatibility rules for ATLAS during the design and installation phases of the calorimeters and of their electronics. This has been particularly demanding for the LAr cryostats, since all services, such as cryogenic lines, cooling pipes, etc., and all mechanical connections to the surrounding detector systems had to be installed in a way which preserved the electrical isolation of the cryostats. The most difficult challenge has been related to the large amount of pipes which run along the cryostat walls and enter the inner bore of the barrel cryostat to service the inner detector. The cryostat surfaces are wrapped in insulating foils or covered by thin glass-fibre sheets to prevent any accidental electrical contact. Concerning the calorimeter electrical connections, the DC isolation of the power to the front-end boards is taken care of by the DC-DC converters of the low-voltage power supplies (see section 5.6.3.1). The shields of all cables connected to the cryostats are interrupted at one end. For example, the shield of the L1 cables (the only copper links in the calorimeter readout) is disconnected at the entrance of the receiver boards. The cryostats themselves are connected to the safety ground [127] by long cables with a large copper cross-section to a single point close to the L1 receiver racks. This choice minimises the potential difference between the analogue sending and receiving ends of the trigger signals. The tile calorimeter itself is structurally supported on rails which are grounded to the cavern safety network. Additionally, dedicated grounding cable connections for each of the three tile calorimeter barrels are made to the cavern network [128].

5.6.1.2 LAr calorimeter front-end electronics

The sensitive analogue electronics [125] are located on the detector. Inside the cryostat, the calorimeter electrodes are grouped to form readout cells and small coaxial cables bring the cell signals to the cold-to-warm feed-throughs (see section 5.4), except for the HEC (see section 5.3.2). Custom front-end crates are mounted near the feed-throughs and contain several types of boards:

1. The calibration board [129] injects precisely known current pulses through high-precision resistors to simulate as accurately as feasible energy deposits in the calorimeters. These resistors are mounted on the detector in the cold for the barrel and end-cap electromagnetic calorimeters and for the HEC, and mounted on the base-plane of the front-end crates for the FCal (see section 5.6.2).
2. Front-end boards [130] (FEB) receive the raw calorimeter signals and, as described in more detail below, perform the analogue processing, digitisation and transmission off-detector of the calorimeter signals.

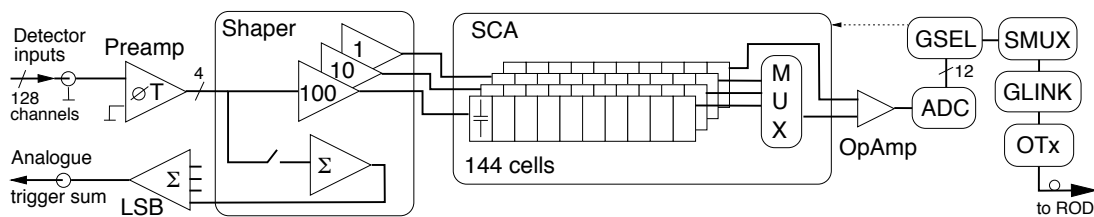


Figure 5.29: Block diagram of the FEB architecture, depicting the dataflow for four of the 128 channels (see text for details).

3. Tower-builder boards perform the final level of analogue summation for the barrel and end-cap electromagnetic calorimeters to form trigger-tower signals and transmit the analogue signals to the L1 trigger processor, where they are digitised and processed. The corresponding boards which transmit the HEC and FCal trigger towers are called tower-driver boards, since no summation is performed in this case.
4. Front-end crate-controller boards receive and distribute the 40 MHz clock, the L1 trigger accept signal, as well as other fast synchronous signals and information to configure and control the front-end electronics boards (SPAC protocol).
5. Additional boards transmit the information from the mechanical sensors monitoring possible stresses of the detector, from the temperature gauges situated in the liquid argon, and from the purity monitors.

A total of 58 front-end crates are needed to read out the complete LAr calorimeter system. The configuration of such a crate is typically the following (e.g. for the barrel electromagnetic calorimeter): 28 FEB's and two each of the calibration, trigger-tower builder and front-end crate controller boards described above.

The analogue processing and digitisation of the calorimeter signals is performed by the FEB's. Each FEB processes up to 128 calorimeter channels, and a total of 1524 FEB's are used to read out the 182,468 channels of LAr calorimetry. A block diagram indicating the main features of the FEB architecture is shown in figure 5.29. The raw signals from the calorimeter are mapped onto the FEB inputs as they emerge from the cryostat feed-throughs. Four-channel preamplifier hybrids amplify these raw signals (in the specific case of the HEC, preamplifiers mounted on the detector and operating in the cold provide some amplification of the signals before they reach the FEB's). The preamplifier outputs are AC-coupled into a four-channel shaper ASIC, which splits each signal into three overlapping, linear gain scales in the ratio 1/10/100, and applies a bipolar $CR - (RC)^2$ analogue filter to each scale to optimise the signal-to-noise ratio. The single differentiation step serves to remove the long tail from the detector response, while the two integrations limit the bandwidth in order to reduce the noise. The time constant is chosen to be 15 ns to minimise the overall noise level, as a compromise between the two main contributions, namely electronic noise and pile-up noise, which respectively decrease and increase with the shaping time. This value is optimised for a luminosity of $10^{34} \text{ cm}^{-2} \text{ s}^{-1}$. The triangular input current pulse from the detector and the shaped output pulse from the FEB are depicted for the case of a barrel electromagnetic cell in figure 5.30.

The shaped signals are then sampled at the LHC bunch-crossing frequency of 40 MHz by four-channel switched-capacitor array (SCA) analogue pipeline ASIC's. The SCA stores the analogue signals during the L1 trigger latency in pipelines of 144 cells, and also serves as a multiplexer and de-randomising buffer in front of the ADC for triggered events.

For events accepted by the L1 trigger, typically five samples per channel and only one of the three gain scales are read out from the SCA. A gain-selector chip (GSEL) is used to select the optimal readout gain individually for each calorimeter channel and separately for each L1 trigger. Two commercial dual op-amp chips couple the SCA outputs to commercial 12-bit ADC's used for the digitisation of the analogue signals. The signals are formatted by the GSEL, multiplexed (SMUX), serialised at 1.6 Gbits/s (GLINK), and then transmitted via a single optical transmitter (OTx) based on vertical-cavity surface-emitting laser diodes (VCSEL).

Each shaper ASIC contains an analogue summing circuit, which sums its four channels as the first step in producing sums for the L1 trigger system. Channels can be individually enabled or disabled during FEB configuration in order to mask noisy channels. The four-channel sums are routed on the FEB to plug-in boards, which contain the next stage of the trigger analogue summing tree and which drive their output sums through the crate back-plane to the tower-builder (or tower-driver) boards, where the sums are completed before transmission off-detector to the L1 trigger system.

5.6.1.3 Tile calorimeter front-end electronics

The front-end electronics of the tile calorimeter are housed inside drawers located within the steel girders which constitute the external support frame of the tile-calorimeter modules (see section 5.3.1.1). A block diagram of the tile-calorimeter front-end electronics and readout components inside the drawer is shown in figure 5.31.

A key element in the readout is the photomultiplier (PMT) block [131]. It is a mechanical structure comprising a steel cylinder and mu-metal shield for magnetic shielding, which contains a light mixer, a photomultiplier tube, a voltage divider and the so-called 3-in-1 card. The light mixer is an optical plastic insert which mixes the light from the readout fibres to ensure uniform illumination of the photo-cathode. The PMT's with their compact 8-dynode structure are used to measure the scintillation light [132]. All PMT's were burned in and tested for linearity, stability, dark current and operating voltage for a nominal gain of 10^5 [112]. The average operating voltage for nominal gain is 680 V. The assembled PMT blocks are inserted inside precision slots inside the aluminium structure of the drawers, which ensure accurate placement of the light mixer relative to the fibre bundle for each readout cell.

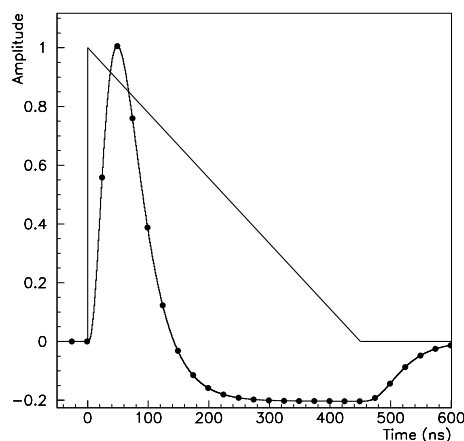


Figure 5.30: Amplitude versus time for triangular pulse of the current in a LAr barrel electromagnetic cell and of the FEB output signal after bi-polar shaping. Also indicated are the sampling points every 25 ns.

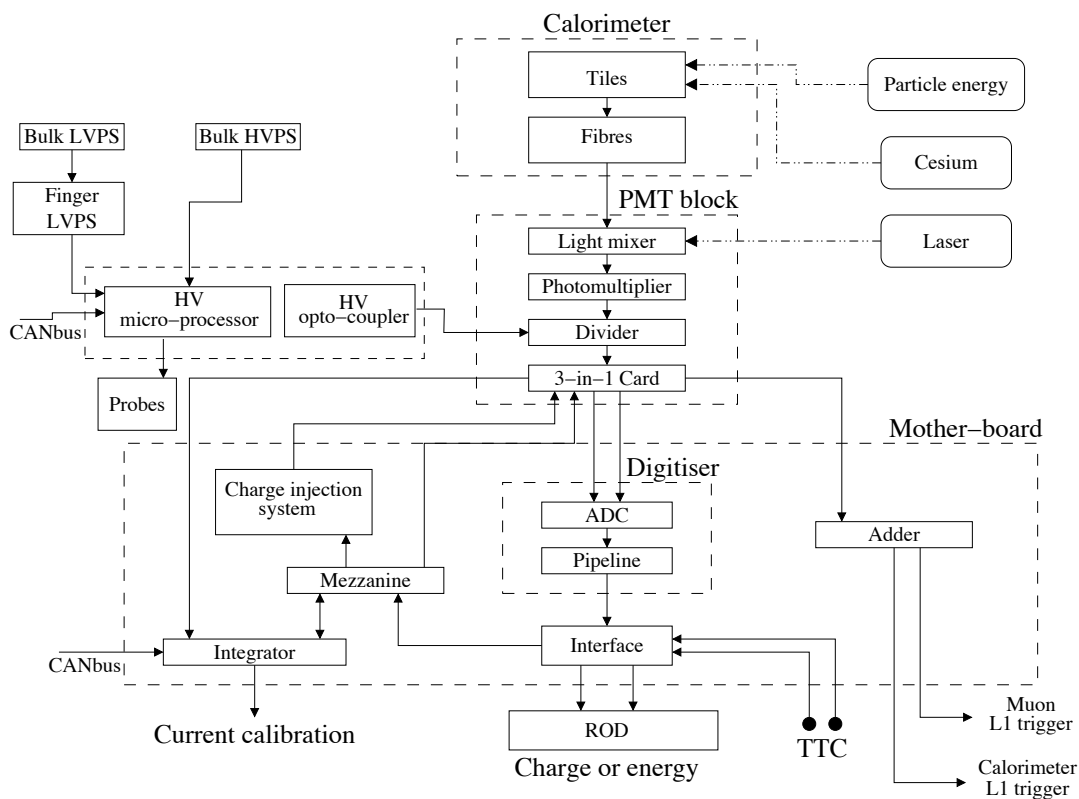


Figure 5.31: Block diagram of tile-calorimeter readout electronics.

The high voltage for each PMT is regulated with an accuracy of better than 0.25 V by micro-controllers inside the drawer. A single micro-controller services up to 48 PMT channels and has a memory into which the nominal and set values of the voltage for each PMT are loaded. Each high-voltage distributor system drives seven temperature probes located at key locations inside each drawer.

Most analogue functions of the front-end electronics are contained on the 3-in-1 card [133]. This board provides unipolar signal shaping to yield a pulswidth of 50 ns and two linear outputs with a relative gain of 64 to achieve the overall 16-bit dynamic range required. The full scale on the low-gain channel corresponds to 800 pC (the PMT gain is adjusted to provide approximately 1 pC/GeV). Charge-averaging amplifiers on the 3-in-1 card are used for cell calibration and monitoring and a charge-injection system is incorporated to calibrate the readout over its full dynamic range. The 3-in-1 card also produces the analogue signals for the L1 trigger.

The digitiser system [134] samples the incoming data from the 3-in-1 cards every 25 ns using two dedicated 10 bit ADCs (one for each of the low-gain and high-gain channels) and stores the information in a fixed-length pipeline, while waiting for a L1 trigger accept (L1A). Each digitiser services up to six PMT channels. Each triggered event is recorded over an extended time frame, with a programmable length of up to 16 samples. In normal data-taking mode, following a L1A signal, seven samples are kept: one close to the peak, four before the peak (with the two first samples providing a measurement of the signal pedestal) and two after the peak.

There is one interface board [135] per pair of drawers. It receives and distributes the timing, trigger and control (TTC) signals, collects and formats data from the digitiser cards, and transmits the digitised data via an optical link. The interface board also performs cyclic redundancy checks on the input and output datastreams.

A system of four linked mother-boards form the base of the readout system. They distribute power to the 3-in-1 cards, the ADC integrator, the mezzanine card and the adders. Each mother-board also contains circuitry which generates a precise reference voltage used by the 3-in-1 cards for charge injection and integrator calibration. The mezzanine card is mounted on the first mother-board in the drawer. It decodes control commands sent via the TTC system and sends them on differential serial lines to the 3-in-1 cards. These commands control the charge injection, integrator gain setting and calibration, trigger-output gating and integrator bus access for each 3-in-1 card. The mezzanine card can also receive commands via the ADC integrator card, which is mounted on the first mother-board. It sends and receives messages via a dedicated CANbus daisy chain. The micro-processor in the ADC integrator card queues commands to the mezzanine card. It sets the integrator gain on a 3-in-1 card, multiplexes the 3-in-1 card onto the integrator readout bus and reads out the charge induced by the cesium source, by minimum-bias events, or by the on-board calibration DAC. The ADC integrator can also read back 3-in-1 card status and control information.

Adder boards [136] are distributed along the drawer mounted on the mother-boards. Each adder board receives the analogue trigger outputs from up to six 3-in-1 cards. The inputs are connected to form trigger towers. The adders perform an analogue sum of the input signals and send two output signals via long cables to the L1 trigger system. One of these signals (tower signal) comprises the sum of all samples, the second one (muon output) contains only the last tile-calorimeter sampling. In the case of the gap and crack scintillators (see section 5.5), the adder board provides amplification to match the small signals from these scintillators to the signal amplitudes required by the L1 trigger boards. It also provides the sum of the signal in all four of the gap and crack scintillators. The muon output from these adder boards (see figure 5.31) provides the signal from the scintillator covering the region $1.2 < |\eta| < 1.4$. As mentioned in section 5.5, sixteen of these channels will be used for the trigger from the minimum-bias trigger scintillators during initial data-taking.

5.6.1.4 Back-end electronics

Overview of architecture. The back-end system [126, 137] for all calorimeters is housed in the main services cavern (USA15), located 70 m away from the detector, and contains three different sub-systems: the readout driver (ROD) system, which constitutes the core of the back-end, the trigger, timing and control (TTC) system, and the L1 trigger receiver. The back-end system reads the data from the front-end electronics, and digitally processes the data before transmitting it to the data acquisition system at a L1 trigger rate of up to 75 kHz for the physics data-taking mode and at a 10 kHz rate for the calibration mode. The back-end system also receives the TTC signals, distributes the timing clock and trigger to the front-end electronics and the ROD's, and configures and controls the front-end crates. All of these tasks must be performed fast enough to cope with the above trigger rates.

The ROD's are responsible for receiving, digitally processing and formatting the data from the front-end electronics and for performing various data-integrity checks and higher-level monitoring tasks. The ROD module comprises a ROD mother-board on which are plugged up to four processing-unit mezzanine cards. Each processing unit houses two commercial Digital Signal Processor (DSP) chips operating at 720 MHz. Each DSP is preceded by an input buffer used to perform data-integrity checks as well as to reformat the input data to suit the DSP architecture. Following each DSP is an output buffer used to buffer processed events before transfer to the data acquisition system. For each trigger, data from the TTC stream and from the front-end electronics are pushed into the ROD modules, where they are checked, processed, formatted and sent on a readout link to the ATLAS data acquisition system.

Optimal filtering. The most important task of the DSP is to apply an optimal-filtering method to the signals, including the relevant calibration constants, in order to provide the deposited energy (in GeV) and the signal timing (in ns) for each cell [138]. This optimal-filtering method is at the core of the back-end processing role and has been implemented in all the calorimeter ROD's. It calculates the energy E , the timing τ and a simplified χ^2 for the shaped and digitised signal from each cell, by means of a weighted sum over the relevant sample amplitudes, s_i , expressed as:

$$E = \sum_{i=1}^n a_i(s_i - ped) \quad E\tau = \sum_{i=1}^n b_i(s_i - ped) \quad \chi^2 = \sum_{i=1}^n (s_i - ped - E(g_i - \tau g'_i))^2, \quad (5.1)$$

where n is the number of samples and ped is the pedestal value of the corresponding readout channel, and g_i and g'_i are respectively the normalised ionisation pulse shape and its derivative with time. The optimal filtering weights, a_i and b_i , are evaluated while minimising the dispersion in E and $E\tau$ arising from electronics and pile-up noise, taking into account the noise auto-correlation matrix and the pulse shape at the input of the digitiser.

Trigger, timing and control. Four VME crates are used to implement the timing trigger and control (TTC) system, where up to two partitions are implemented in a single crate. Each TTC partition contains a controller and a local trigger processor (see section 8.2.3 and figure 8.12).

The trigger latency, which is the delay between the bunch-crossing time and the time when the L1 accept signal (L1A) arrives to the front-end electronics, has been minimised to a value below $2.5 \mu\text{s}$. The TTC rack location has been chosen to minimise the length of the TTC fibres to the front-end crates and the associated contribution to the trigger latency. In addition, the programmable delay lines of the calibration boards are preset to reproduce the timing of signals generated by particles originating from the interaction point.

Receiver system. The receiver system is part of the trigger-sum chain and interfaces the tower-builder and tower-driver boards to the calorimeter L1 processor. One important function of the trigger-sum chain is to convert the signal from energy to transverse energy. The final gain adjustment is left to the receiver. Each receiver crate contains 16 receiver modules, two monitoring modules and one controller module. The LAr system consists of six receiver crates: two for the barrel electromagnetic, two for the EMEC's and two for the HEC and FCal. Two additional crates are for the tile calorimeters.

LAr back-end electronics. As described above, the optimal-filtering method calculates the energy for each cell while minimising the noise and pile-up contributions. For cells with an energy above a certain threshold (approximately 5% to 10% of all cells), the precise timing of the signal as well as a χ^2 -like quality factor, allowing to flag cells with a large pile-up contribution, are determined and transmitted as well. For an even lower fraction of cells, the individual samples are also transmitted.

The pulse after the bipolar shaping is sampled every 25 ns (see figure 5.30). For normal data-taking, five samples are typically used, whereas for calibration and commissioning, up to 32 samples can be taken. The energy E , time τ and simplified χ^2 of the signal pulse are calculated as in eq. (5.1). The values g_i and g'_i are estimated in different ways for the various calorimeters, using a number of methods: the pulse-shapes measured in test-beam, the measured calibration pulse, and a detailed modeling of the front-end electronics and readout chain [126]. These methods must take into account the different signal injection points used in the different calorimeters and the differences between the shapes of the ionisation and calibration signals.

As an illustration, figure 5.32 shows the variation of the noise with the number of samples, as obtained in situ for the strip and middle layers of the barrel electromagnetic calorimeter. For the chosen number of five samples used in the back-end for normal LHC operation, the electronic noise is reduced by a factor ~ 1.7 with respect to a readout which would use only one sample.

To increase modularity and allow for concurrent running of the various parts, the LAr calorimetry is split into six partitions: one for each half-barrel, one for each EMEC, and one for HEC and FCal on a given side. Each partition is associated to a computer, which controls and monitors the system, and to a TTC sub-system. A typical barrel partition (see [126] for the configuration of the other partitions) is composed of four ROD crates and the associated front-end electronics. Each ROD crate contains 14 ROD boards and drives and controls four front-end crates.

Tile calorimeter back-end electronics. In addition to the ROD system described above, modified slightly to have two rather than four processing units per ROD board, the tile-calorimeter back-end electronics system also includes an optical multiplexer board [139]. This board has the responsibility of checking data coming from the front-end electronics. There are two fibres per front-end drawer carrying the same data and the board selects the error-free one in real time by checking the integrity of the data received using a cyclic redundancy check. It can also act as data injector for the ROD system.

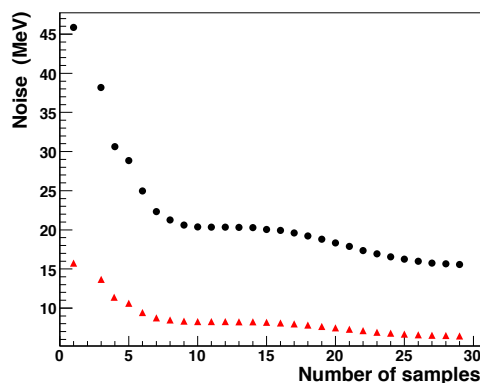


Figure 5.32: Plot of the electronic noise in the electromagnetic barrel as a function of the number of readout samples. The circles correspond to a middle-layer cell and the triangles to a strip-layer cell. For the case of five readout samples, as planned for normal data-taking, the electronic noise is reduced by a factor of ~ 1.7 compared to the case of only one readout sample.

The ROD system of the tile calorimeter is physically divided into four independent partitions, two for the readout of the barrel calorimeter and one for each extended barrel calorimeter. Each partition is composed of a 6U VME TTC crate and a 9U VME ROD crate (containing eight ROD processing-unit boards), which read out up to 64 front-end drawers. The ROD processing unit performs various data-integrity checks and reconstructs the amplitudes of the digitised signals using the optimal-filtering method described above. Several algorithms based on optimal filtering are being developed to deal with detector and pile-up noise. The optimal-filtering method is also used to reconstruct the signal in charge-injection calibration runs.

5.6.2 Calorimeter calibration systems

The LAr and tile calorimeters have very precise charge-injection systems and calibration boards to calibrate the response of the front-end electronics boards. The tile calorimeter is equipped with two additional calibration systems to monitor the behaviour with time of the photomultipliers and of the optical components.

5.6.2.1 Calibration of LAr calorimeters

The aim of the electronic calibration is to determine the conversion factor, expressed as the ratio between the measured signal in ADC counts to the signal current in μA , for each individual channel and to monitor this factor with time.

The use of fast shaping for the calorimeter readout requires that the distribution of the calibration signals be done via injection resistors directly placed at the input of the detector cell and not at the input of the preamplifier located outside the cryostat. This is shown in figure 5.33 for the barrel and end-cap electromagnetic calorimeters for which the greatest precision is required. In the case of the HEC, the calibration pulse is injected in front of the cold preamplifiers. In the case of the FCal, however, the calibration pulses are applied at the base-plane of the front-end crates, where the signals are split into two. One of the split pulses goes directly into the front-end boards and the other goes through the cold electronics chain, reflects off the electrodes and is observed as a delayed pulse. The direct pulses are used to calibrate the electronics in the front-end crates and the delayed pulses are used to examine problems related to the FCal and its cold electronics.

The conversion of the signal in μA to a signal in GeV has been obtained for all LAr calorimeters from test-beam measurements. Figure 5.34 shows these conversions factors for the electromagnetic calorimeters. This factor only changes once in the barrel when the absorber thickness changes at $|\eta| = 0.8$, whereas it changes almost continuously in the end-cap calorimeter because of the geometry and of the varying high-voltage. For the presampler cell energy scale, an effective sampling fraction has been applied with a value of 1/20 for the barrel and of 1/60 for the EMEC. These values correspond approximately to the weights which have to be applied to the presampler signal to correct for the energy loss of electrons before reaching the calorimeter. The conversion factors in figure 5.34 agree with predictions based on Geant 4 simulations and knowledge of the LAr ionisation energy and drift velocity [140].

In the HEC1 wheel, this conversion factor is $0.306 \mu\text{A}/\text{GeV}$ and it is half that value for HEC2 with its twice thicker absorber plates. The corresponding conversion factors for the FCal are 1.49, 0.69 and $0.64 \mu\text{A}/\text{GeV}$, respectively for FCal1, FCal2 and FCal3.

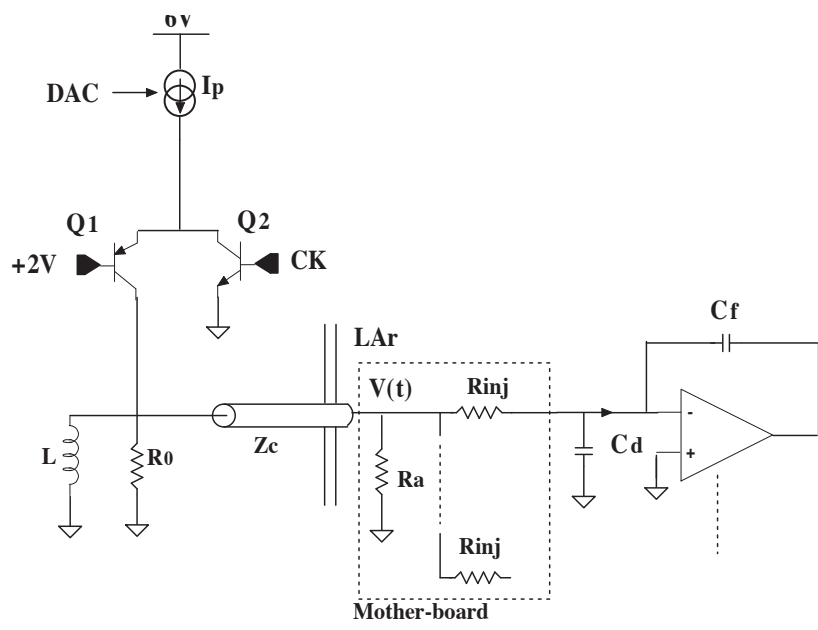


Figure 5.33: Schematic diagram of the calibration system for the LAr electromagnetic calorimeters. The components in the left part of the diagram are located on the calibration board itself at ambient temperature in the front-end crates, whereas the right part of the diagram depicts the distribution of the calibration signal into the calorimeter cells. This is achieved through the precision resistors (R_{inj}), which are located on printed-circuit boards in the liquid argon. The impedance of the cable between the calibration board and the printed-circuit boards in the liquid argon is denoted Z_c .

The calibration boards [129] are built to deliver a uniform, stable, linear and precise voltage-driven signal with an amplitude and shape as close as possible to the calorimeter ionisation current signal over a 16-bit dynamic range (with currents up to 100 mA over 50Ω). The triangular ionisation pulse is in practice approximated by an exponential shape. The chosen distribution scheme, typically one calibration channel every four signal channels, also allows the measurement of cross-talk [140]. The largest cross-talk is between neighbouring strips in the first layer of the electromagnetic calorimeter. It amounts to 5 – 8% and is corrected for in the strip energy measurement. The calibration boards are equipped with programmable delays which are used to compensate the timing differences due to the cable lengths. Apart from pedestal and gain measurements, a mea-

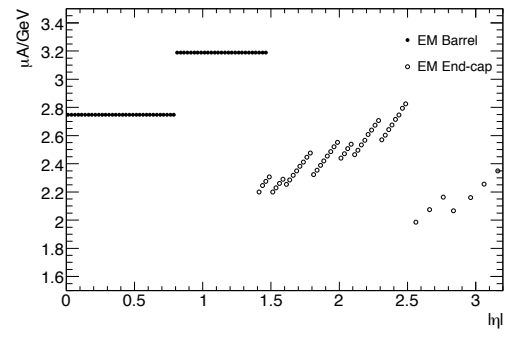


Figure 5.34: Initial ionisation current per deposited energy from electromagnetic showers in the barrel and end-cap electromagnetic calorimeters. These values have been derived from electron test-beam data.

surement of the pulse shape is performed by precisely delaying the trigger, using the TTCrx chip located on the calibration board. A total of 132 calibration boards have been produced. They fulfill the required performance of an integral linearity better than 0.1%, a uniformity better than 0.2%, and a stability as a function of time better than 0.1%.

In the computation of the calibration constants for the electromagnetic calorimeter, however, a small difference in the response between physics and calibration pulses for the same initial current should also be taken into account. This arises from the different injection points of the current (see figure 5.33) and from the difference between the exponential current as a function of time for the calibration and the triangular pulse shape of the physics pulse (see figure 5.30). This difference depends on the electrical properties of the readout cells and on pseudorapidity and never exceeds 4%. The procedure to compute this correction has been validated during the study of the response uniformity with test-beam data of production modules. For this reason, several calibration methods have been used to determine the optimal-filtering coefficients (see section 5.6.1.4).

5.6.2.2 Calibration of tile calorimeter

Each tile-calorimeter cell can be divided into three sections for calibration purposes; the optical part consisting of scintillator and fibres, the photomultipliers, and the front-end electronics which shape and digitise the light signals. A calibration and monitoring system is used to certify each of these parts independently [141].

The charge-injection system is designed to calibrate the front-end shaping and digitising circuits to an accuracy of 1%. It uses a precision DAC on each of the 3-in-1 cards, in conjunction with solid-state switches and precision capacitors. Dedicated charge-injection runs are taken scanning the full range of both gains. Fits to the measured pulses convert ADC counts to pC and yield a typical non-linearity of about two ADC counts over the full dynamic range, with a stability of better than 1% over many months of monitoring.

The laser system is used to calibrate and monitor the photomultiplier response with a target accuracy of better than $\pm 1\%$. This system sees both the front-end electronics and the photomultipliers. A Nd:YVO4 laser, synchronised to the TTC clock generates pulses of ~ 10 ns length at a wavelength of 532 nm. The laser light is split in the main services cavern (USA15) and sent via clear plastic fibres to each calorimeter finger where it is again split to each photocathode. The pulse-to-pulse variation is monitored at the laser by several pin-diodes and, by means of a filter wheel, the laser light intensity can span a dynamic range of 10^4 . The global photomultiplier non-linearity is found to be $< 0.5\%$ above 80 pC and up to where saturation sets in. In addition, the system can be used to set the global calorimeter timing and to investigate saturation-recovery techniques.

To calibrate and monitor the tile-calorimeter scintillator and optical system, a ^{137}Cs γ -source of ~ 10 mCi strength is moved hydraulically inside the calorimeter body. This system sees the full chain from the optical part to the front-end electronics and to the photomultiplier. It enables the setting of the high voltage of each channel and inter-calibration of all the 10000 tile channels. These calibrations are performed during dedicated runs, with the source traversing each of the 463,000 tiles in the detector [142]. The photomultiplier current is integrated by the 3-in-1 cards as the source passes within the corresponding cell. From the digitised current, the response of each

scintillator tile can be extracted. The accuracy of a single tile response is better than $\pm 2\%$, and the mean response accuracy for a calorimeter cell is $\pm 0.3\%$. Based on monitoring a single module over a period of four months, the long-term stability of the system was determined to be 1%. A procedure to set the gains of each photomultiplier based on the integrated cell-source current allows inter-calibration of cells and modules to better than $\pm 3\%$ [141]. The absolute energy calibration (pC/GeV) is set with electrons, as described in section 5.7.4.1.

5.6.3 Calorimeter power supplies and services

This section describes briefly the LAr and tile calorimeter power supplies, cooling systems and controls.

5.6.3.1 Low-voltage power supplies

The low-voltage power supplies for the LAr and tile calorimeters are located in the main cavern, as close as feasible to the on-detector electronics boards. To this end, they had to be custom built and validated to operate in a high radiation environment, in a significant residual magnetic field of up to 100 mT, and in a very limited volume.

Each front-end crate of the LAr calorimeter is powered by a low-voltage power supply located close to it in the gap between the cryostats. This power supply delivers with multiple, redundant DC-DC converters, the seven DC voltages necessary to the front-end crate. There are a total of 58 low-voltage power supplies, 2×16 for the barrel electromagnetic calorimeter and 2×13 for the end-cap calorimeters. Each low-voltage power supply is powered by a 280 V DC power supply located in the underground counting room (USA15). The low-voltage power supplies and associated 280 V power supplies are controlled and monitored using a custom interface board, ELMB, described in section 8.5.

Low-voltage power to the tile-calorimeter drawer electronics is supplied by a custom power supply located in a mechanical extension on the ends of the module. These extensions are located on either side of the central barrel and on the outer surface of each extended barrel at the support girder. Each water-cooled power supply consists of eight isolated switching DC-to-DC convertors (bricks) which are powered by a customised external 200 V DC bulk power supply. The bricks themselves are controlled and monitored at two levels externally through CANbus using a custom interface board based on the ELMB described in section 8.5 and using current loops. An independent external reset from USA15 is available in the case of a failure in the voltage control network (for example due to a single event upset). A second auxiliary board, also based on the ELMB and located in USA15, provides overall control.

5.6.3.2 High-voltage power supplies

High voltage is delivered to the LAr and tile calorimeters through commercial or custom-built external power supplies located in the underground counting room.

Several different versions of the same industrial power supply are used to power the different LAr detectors, according to the voltage and current needed. The maximum voltage and current of each version are given in table 5.6. Furthermore, the barrel electromagnetic, EMEC or HEC

Table 5.6: Nominal voltages, maximum voltage and maximum current of the different LAr calorimeter high-voltage power supplies.

Detector	Nominal detector voltage (V)	Maximum module voltage (V)	Maximum module current (μA)
Electromagnetic barrel	2000	2500	75
Barrel presampler	2000	2500	75
Electromagnetic end-cap (EMEC)	1000 to 1700	2000	200
	1800 to 2500	2500	200
End-cap presampler	-2000	-2500	75
Hadronic end-cap (HEC)	1800	2500	75
Forward calorimeter (FCal)	250, 375, 500	600	6000
Purity monitors	± 2500	± 2500	75

channels showing a problem, such as a resistive short, are powered by high-current (maximum of 3 mA) supplies. A power supply module contains two boards with 8 (FCal) or 16 (all detectors but FCal) channels each. All high-voltage channel parameters can be controlled remotely and in particular the voltage itself, the ramp speed and the trip levels for the current drawn. In total, there are 157 modules housed in 20 crates containing eight modules each for the whole LAr system.

High voltage is delivered to the tile-calorimeter drawers from external bulk power supplies. The supply can deliver two voltages to the input of the drawer (-830 V and -950 V) to match the PMT operating requirements and provides a maximum current of 20 mA. The voltage is distributed inside the drawer and regulated to provide the desired voltage for each PMT. A single bulk supply provides high voltage to 16 drawers.

5.6.3.3 Cryogenics and cooling

The cryogenics services for the LAr calorimeters are described in some detail in section 9.4.5 and shown in figure 9.6. The cooling systems for the LAr and tile calorimeter electronics are both based on a leak-less system for the on-detector implementation (see section 9.4.3 for an overview of the off-detector systems). The cooling system supplies demineralised water at 18°C and works with sub-atmospheric pressure to prevent the cooling liquid from leaking out of the system should a break or holes occur in a cooling pipe.

The total consumption of the LAr front-end readout electronics exceeds 200 kW (each FEB channel has a consumption of $\sim 0.7\text{ W}$). Therefore, each electronic board in a front-end crate is conductively cooled using two aluminium plates placed on each side of the board. These aluminium plates are implemented as part of the leak-less cooling system. The temperature of a FEB is maintained constant at $\pm 1^\circ\text{C}$. Under these conditions, no temperature dependence is observed on the pedestals, the gains and the delays of the readout electronics. The low-voltage power supplies are also operated using the same cooling system.

A heat dissipation of 300 W is expected from a pair of tile-calorimeter drawers and a leak-less cooling system [143] provides cooling inside the drawers. The performance requirements were determined with a prototype system [144] which was used during the calibration of production modules in a test-beam. By varying the input temperature and flow-rate it was possible to

change the temperature inside the drawer while measuring the response of the calorimeter to a high-energy pion beam. The fractional energy variation as a function of temperature changes of the PMT block was found to be $0.2\%/^{\circ}\text{C}$ and the variation in response of the PMT gain itself as a function of temperature changes of the cooling water is $0.15\%/^{\circ}\text{C}$. To ensure a PMT gain stability of $\pm 0.5\%$, the temperature variations of the PMT block must be smaller than $\pm 2.5^{\circ}\text{C}$. Long-term tests carried out during calibration of production modules showed that the system could maintain the temperature in a drawer to within $\pm 0.3^{\circ}\text{C}$.

5.6.3.4 Detector control systems

Within the context of the overall ATLAS detector safety (DSS) and control (DCS) systems described in section 8.5, this section describes the main operating parameters monitored by the specific DCS implementations of the different calorimeter systems.

LAr controls. The LAr DCS controls and monitors two important operational parameters: the liquid-argon temperature and purity.

- **Temperature measurements**

The measured sensitivity [140] of the LAr signal to temperature is -2% per degree. Numerous calibrated ($\Delta T = 10$ mK) temperature probes (PT100 platinum resistors) have therefore been installed in each calorimeter to measure precisely the liquid-argon temperature. A total of 192 temperature probes are glued on the absorbers of the barrel electromagnetic calorimeter at two radii (inner and outer) and regularly distributed in $z \times \phi$ (6×32). Similarly, a total of 32 (respectively 18) temperature probes are located at the front and back sides of the external (respectively internal) EMEC wheels, close to their outer radius. These probes are also uniformly distributed in ϕ .

A total of 192 HEC temperature probes fixed on copper blocks at three radii (inner, middle and outer) are located near the HEC-wheel rear surface and uniformly distributed in ϕ . Finally, the three FCal modules are equipped with a total of 14 temperature probes, four at the outer radius and ten at the inner radius, where heating from beam interactions and heat transfer through the cryostat wall is highest. These sets of temperature probes are completed by other sets, used to control and monitor the temperature during the cooling or heating of the cryostats.

- **Purity monitors**

To control the argon purity, ten purity monitors have been installed on the outer radius of the barrel calorimeter between the support rings. They are located in the median azimuthal plane and at the top and the bottom of the half-barrels. Ten purity monitors are also installed in each end-cap cryostat, two in the EMEC region, six in the HEC region and two in the FCal region. The impurity measurement is based on the energy deposition by radioactive sources in the liquid argon. The ionisation charge is collected by an electric field and measured by a cold pre-amplifier. Each device consists of two radioactive sources: an ^{241}Am source, which emits 5.5 MeV α -particles, and a ^{207}Bi source, which emits 1 MeV conversion electrons.

The ratio of the measured charges between the Bi and Am sources is used to extract the absolute oxygen content in the liquid argon [107]. The oxygen contamination in the barrel LAr cryostat has been monitored to remain below 0.3 ppm since more than a year of cold operation in the ATLAS pit and is stable to better than a few %. The argon purity achieved is thus well within specification.

The other quantities controlled and monitored by the LAr DCS are mainly concerned with the readout electronics. On the detectors, DCS controls also the voltage, the current and the temperature of the HEC front-end power supplies. On the high-voltage system, DCS controls the voltage, the intensity and the pre-set value for switching off each high-voltage channel. The temperature of each high-voltage module is also monitored. On the front-end electronics, DCS controls the power supplies and monitors the voltage, the current and the status of the 280 V power supplies, which powers the front-end crates, and of the low-voltage power supplies in the front-end crates (the temperature of each FEB is monitored by the DAQ system). Finally, on the back-end electronics, DCS monitors the voltage, the current and the temperature of each crate.

Tile controls. The tile-calorimeter DCS controls and monitors mainly the on-detector low-voltage and high-voltage power supplies and electronics cooling, as well as the off-detector high-voltage and bulk 200 V DC power supplies, auxiliary boards and electronics racks. The communication with the high-voltage bulk power-supply crates is done using RS422. CANbus is used for the communication with the micro-controller cards located on the high-voltage side of the drawers. A client-server system has been developed and commissioned for the control and monitoring of the photomultiplier high voltages. Control and monitoring of the on-detector low-voltage power supplies is implemented via a custom auxiliary board, which multiplexes currents and temperatures from sensors inside the drawers, and communicates via CANbus. The 200 V DC power supplies are controlled and monitored using Modbus.

A total of more than 30,000 parameters are monitored in this system. Configuration data such as system structure (lists and hierarchies of devices), device properties (configuration of archiving, smoothing, etc.) and settings (output values, alert limits) are stored in the configuration database. The data produced is stored in the DCS ORACLE-based archive. Due to the large amount of data monitored by DCS, smoothing is applied to reduce the amount of data stored. A subset of these data (for example photomultiplier high-voltage settings) is also available to offline reconstruction.

5.7 Test-beam measurements and results

5.7.1 Electromagnetic module performance

Four (of 32) barrel and three (of 16) end-cap production modules have been exposed to test-beams with a set-up which includes a cryostat on a moveable table, enabling detailed position scans. These tests have been carried out in the CERN SPS H8 and H6 beam lines, using electron and positron beams of energies between 1 and 250 GeV. A comprehensive analysis of module performance has been reported [140, 145, 146].

The electron energy reconstruction procedure is similar to that described in section 10.4: for example, for the barrel electromagnetic calorimeter, an electron cluster is first constructed using

the measurements in the middle accordion layer, where cells within a square window of 3×3 cells around the cell with the highest energy are clustered together. For the other accordion layers, all cells intersecting the geometrical projection of this square window are included. The energy in each layer, E_0 for the presampler and E_1 , E_2 , E_3 for the strip, middle and back layers, is the sum of the energies of the selected cells in the cluster. The energy of the electron is then given by the algorithm:

$$E = \text{offset} + w_0 \times E_0 + w_{01} \times \sqrt{E_0 E_1} + \lambda(E_1 + E_2 + E_3) + w_3 \times E_3,$$

where the offset and w_0 correct for the energy lost upstream of and in the presampler, w_{01} corrects for the energy deposited in the dead material between the presampler and the strip layer, λ corrects for the energy dependence of the sampling fraction and for lateral leakage outside the electron cluster, and w_3 corrects for the energy deposited downstream of the calorimeter. These coefficients depend somewhat on the electron energy and the η value. An iterative procedure is therefore needed to reconstruct the electron energy. This procedure has been shown to converge after two iterations. The correction coefficients have been determined by simulating the test-beam set-up using GEANT4. In the case of the EMEC, where the presampler is present only in the region $1.5 < |\eta| < 1.8$, where the material in front of the calorimeter was independent of η , and where the beam energy did not exceed 180 GeV, a similar but simplified scheme is used [140].

For the barrel electromagnetic calorimeter, the linearity of the response and the energy resolution have been studied as a function of energy in the range from 10 to 245 GeV at $\eta = 0.687$. At 245 GeV, the beam energy was not known well enough and the linearity of response could not be assessed accurately. The experimental measurements, after noise subtraction, have been fitted with the expression [146]:

$$\frac{\sigma(E)}{E} = \frac{a}{\sqrt{E(\text{GeV})}} \oplus b, \quad (5.2)$$

where a is the stochastic term and b the constant term reflecting local non-uniformities in the response of the calorimeter. In the energy range 15 – 180 GeV, the reconstructed energy response is linear within $\pm 0.1\%$, as shown in figure 5.35. For the lowest-energy point at 10 GeV, a non-linearity of 0.8% is measured. A stochastic term of $10\% \cdot \sqrt{\text{GeV}}$ and a constant term of 0.17% have been obtained from the fit to the fractional energy resolution, as illustrated in figure 5.36. These results are in agreement with dedicated Monte-Carlo simulations of the test-beam set-up. Similar results for the energy resolution have been obtained for the EMEC [110].

At low energy, the calorimeter response to minimum-ionising particles has provided a detailed exploration of the structure of the active material of the detector. In particular, the muon energy deposition is much more localised than the electron energy depositions. Typically, muons only cross one middle cell in η and one or two in ϕ . They can therefore be used to study the fine structure of the calorimeter, without having to deconvolute the effects of the showering process. The signal-to-noise ratio, evaluated as the ratio of the most probable energy deposit divided by the RMS spread of the pedestal, varies between seven and twelve for middle barrel cells and between six and seven for middle end-cap cells. These results have shown that cosmic muons can be used to commission the favourably oriented part of the electromagnetic calorimeters in terms of timing and response uniformity, and may serve to verify the integrity of the detector and of the whole readout chain before the start-up of the LHC [147].

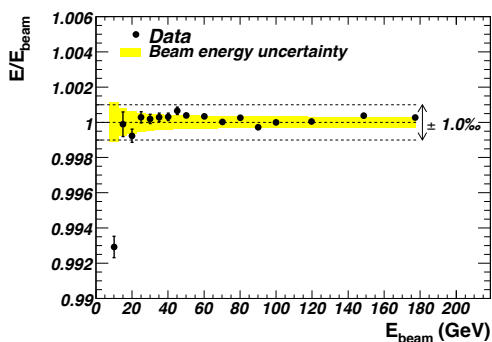


Figure 5.35: Linearity of response as a function of the electron beam energy, E_{beam} , for a barrel LAr electromagnetic module at $|\eta| = 0.687$. All points are normalised to the value measured at $E_{\text{beam}} = 100$ GeV. The band represents the total uncertainty on the beam energy measurement.

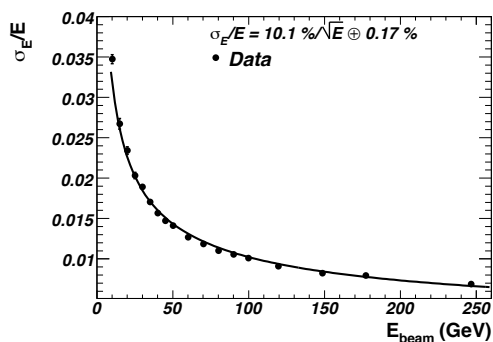


Figure 5.36: Fractional energy resolution as a function of the electron beam energy, E_{beam} , for a barrel LAr electromagnetic module at $|\eta| = 0.687$. Electronic noise was subtracted from the data before plotting the results. The curve represents the results of a fit to the data using eq. 5.2.

The response uniformity at high energy as a function of η has been measured using an electron beam of 245 GeV for the barrel and of 119 GeV for the end-cap [140]. The goal for ATLAS is to achieve a constant term of 0.7% or smaller over the full calorimeter acceptance. Non-uniformities of the response on the tested modules do not exceed 0.7% and do not exceed even 0.5% in the case of the barrel modules, as shown in figure 5.37. The overall constant term in the energy resolution, using the above formula, ranges between 0.5% and 0.7% and therefore meets well the calorimeter design performance goals.

The performance of the barrel electromagnetic calorimeter in terms of its finely segmented first sampling has been studied by using electron, photon and pion beams [145]. The position resolution along η was measured to be about 1.5×10^{-4} and 3.3×10^{-4} (in units of pseudorapidity) at 245 GeV for the front and middle layers, allowing to achieve a polar angle resolution in the range $50\text{--}60(\text{mrad})/\sqrt{E}$ (GeV) over the whole coverage (barrel and end-caps). The π^0 rejection was measured from real data, using a photon beam and mixing together different events to mimic photon pairs from π^0 decays, and found to be 3.54 ± 0.12 (statistical) for π^0 with $p_T = 50$ GeV and for a single photon efficiency of 90%.

A spare electromagnetic barrel module, identical to the series modules, was built for the combined test-beam period described in section 10.1.2 and was exposed to electron, photon, pion and muon beams with energies between 1 and 350 GeV. The amount of material in front of this module was very close to the material expected in ATLAS and therefore great importance was given to the task of verifying that the linearity, energy resolution and uniformity [148] are well understood in terms of the detector description and the simulations using GEANT 4. The performance of the electromagnetic calibration scheme, using longitudinal weights similar to the ones described above, was tested by adding in a controlled way different amounts of material just in front of the electromagnetic calorimeter. This extra material corresponded to 2.4–3.3 X_0 and emulated in this way the material in front of the LAr barrel calorimeter in ATLAS in the region $|\eta| < 1.2$. A linearity

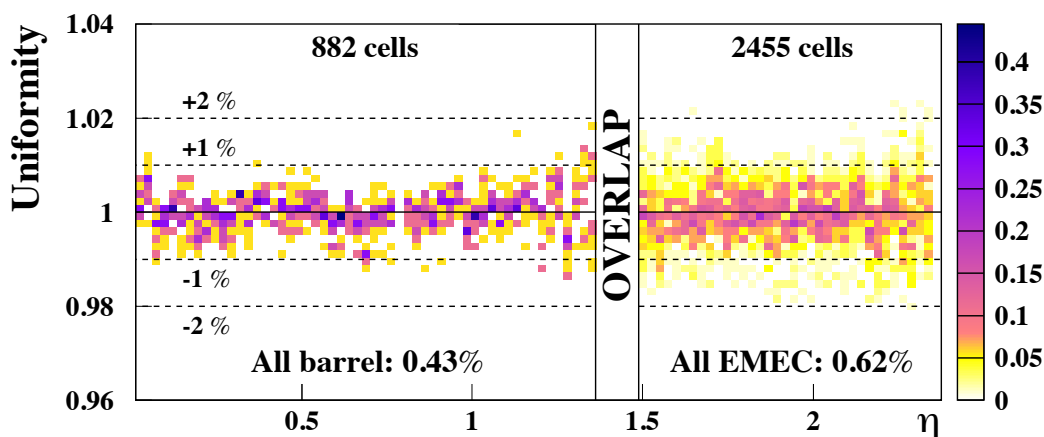


Figure 5.37: Distribution of the average energies measured in all cells of all tested modules as a function of the cell η , normalised to the mean energy measured in the modules. In the barrel, this mean energy was ~ 245 GeV, while it was ~ 120 GeV in the EMEC. For each bin in η , the distribution is normalised to the number of middle cells in that bin (design value). This normalisation is only used to define the colour of each bin in the plot.

of 0.5%, independent of the upstream material, is obtained over the energy range 20–250 GeV, as shown in figure 5.38. Figure 5.39 shows the noise-subtracted ($\sigma_{\text{noise}} = 170$ MeV) resolution at $\eta = 0.4$ for an amount of upstream material of $2.4 X_0$. The data points have been corrected for the beam momentum spread. A stochastic term of $(10.1 \pm 0.4)\% \times \sqrt{\text{GeV}}$ and a constant term of $(0.2 \pm 0.1)\%$ are obtained and the data are well described by the simulation, which incorporates the most detailed and up-to-date description of the detector and GEANT 4 (version 4.8.2) model of electromagnetic showers. More detailed results from this last test-beam period for the barrel LAr electromagnetic calorimetry can be found in [149].

5.7.2 Hadronic end-cap performance

About 25% of the series production modules were exposed to beams of muons, electrons and pions with energies up to 200 GeV at the CERN SPS [150]. Two partial HEC wheels, consisting of three HEC1 and three HEC2 modules were used. The goal was not only to prove the uniformity of the production modules as defined by the hardware tolerances, but also to determine their performance and calibration, as obtained from muons, electrons and pions. The data taken with electrons yield a fractional energy resolution after noise subtraction and a fit to the functional form in eq. (5.2) with a stochastic term, $a = (21.4 \pm 0.1)\% \cdot \sqrt{\text{GeV}}$ and a constant term, b , compatible with zero, in good agreement with predictions from simulation [150]. Horizontal and vertical scans with beams across the surface of the calorimeter showed a homogeneity of the electron signal of $\pm 1\%$ without corrections.

The pion measurements are of particular importance for the prediction of the final performance of the calorimeter for jets. A stochastic term of $(70.6 \pm 1.5)\% \cdot \sqrt{\text{GeV}}$ and a constant term of $(5.8 \pm 0.2)\%$ were obtained from a fit to the functional form in eq. (5.2). The data have

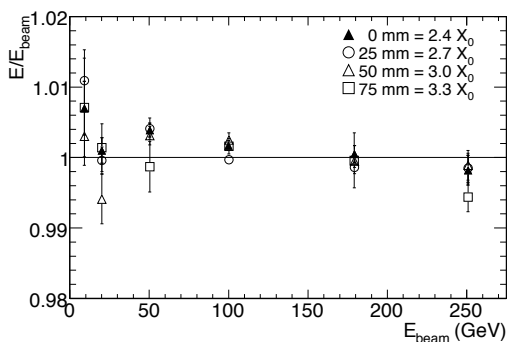


Figure 5.38: Linearity of response as a function of the beam energy, E_{beam} , at $|\eta| = 0.687$, for a barrel LAr electromagnetic module in the combined test-beam set-up exposed to electron beams with different amounts of material placed upstream of the active calorimeter.

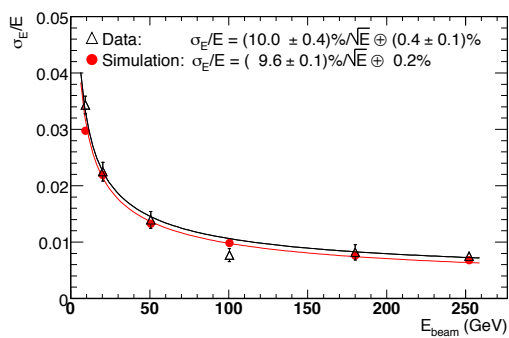


Figure 5.39: Fractional energy resolution as a function of the electron beam energy, E_{beam} , for a barrel LAr electromagnetic module in the combined test-beam. Electronic noise has been subtracted from the data. The results are shown for an amount of upstream material of $2.4 X_0$, which is that expected in ATLAS at $\eta = 0.4$. The curves represent the results of fits to the data and the simulation using eq. 5.2.

been compared in detail to simulations (GFLUKA, GCALOR and GHEISHA) with satisfactory results [151].

From 2002 to 2004, a new set of combined test-beam measurements was launched. The main purposes were to define calibration procedures and constants for initial operation in ATLAS and to operate the EMEC, the HEC and the FCal together in conditions as close as feasible to those expected in ATLAS. The first of these combined test-beam periods took place in 2002 and was devoted to the region $1.6 < |\eta| < 1.8$ [152, 153]. The second period took place in 2004 and was dedicated to a scan of the transition region around $|\eta| = 3.2$.

A three-dimensional clustering algorithm and a signal-weighting approach (see section 10.5.2), used already in previous experiments, have been tested and the first results yield good energy resolution for pions. The signal-weighting technique exploits the fact that local energy depositions of high density are mainly due to electromagnetic interactions, whereas for hadronic interactions, the corresponding density is substantially lower. Thus, for a segmented calorimeter, the energy deposited in individual readout cells can, on a statistical basis, be identified to be of electromagnetic or hadronic origin. For ATLAS, these weights are derived from simulations of single particles and jets. In test-beam, the volume of the related clusters in EMEC and HEC has been used to obtain the cluster energy density. The weighting function has been derived from the data directly, but after correcting for leakage (for details see [152]).

Figure 5.40 shows the energy dependence of the fractional energy resolution separately for the π^- and π^+ data. For energies up to 80 GeV, a differential Cerenkov counter has been used to separate π^+ and protons. The proton contamination in the beam increases with energy and its contribution to the π^+ data in figure 5.40 is the dominant source of systematics when comparing these data to the π^- data and to simulation. Fits to the data using eq. (5.2) yield stochastic terms

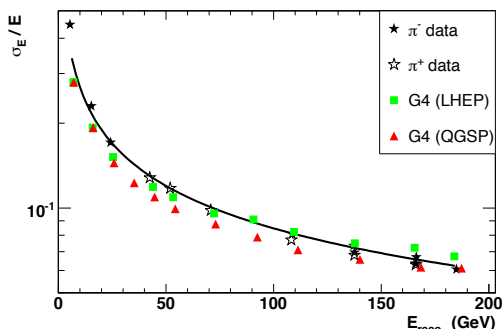


Figure 5.40: Fractional energy resolution as a function of reconstructed energy for π^- and π^+ data taken during the 2002 EMEC/HEC combined test-beam period compared to different predictions from simulation using GEANT 4. The analysis employs the signal-weighting technique described in the text. The data are plotted after noise subtraction and the curve represents as an example a fit to the π^+ data using eq. (5.2).

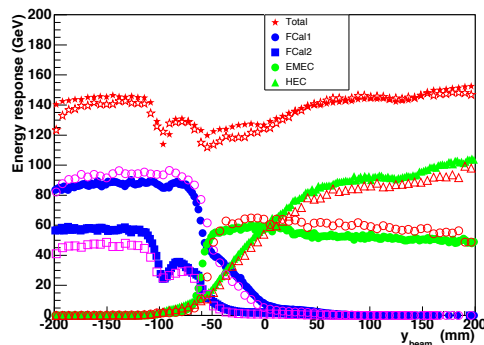


Figure 5.41: Energy response on the electromagnetic scale for 200 GeV pions when performing a vertical scan across the transition region between the EMEC/HEC and FCal calorimeters. Shown is the total energy response together with the individual responses in the different electromagnetic and hadronic components of the calorimetry. The data (full symbols) are compared to GEANT 4 predictions (open symbols).

of $(84.6 \pm 0.3)\% \sqrt{\text{GeV}}$ and of $(81.7 \pm 0.4)\% \sqrt{\text{GeV}}$ for π^- and π^+ respectively, and constant terms of zero within errors. The energy range available is not extensive enough to avoid any correlation between the stochastic and constant terms. Nevertheless, the results give some indication of the effectiveness of the signal-weighting technique in achieving a good level of compensation. The GEANT 4 simulations (version 5.0) with two different hadronic physics lists (LHEP 3.3 and QGSP 2.3) shown in figure 5.40 are in reasonable agreement with the data, but neither model yields an optimal description of the data [151].

The scan of the transition region around $|\eta| = 3.2$ was meant to assess the performance in the complex region of overlap of the three end-cap calorimeters. The EMEC, HEC and FCal modules were positioned as in ATLAS, including mock-ups of the details of cryostat walls and supports (dead material). One quarter of the full HEC1 and HEC2 wheels were assembled with dedicated small modules having reduced η -coverage and encompassing only the forward region. Similarly, one EMEC inner-wheel module (one-eighth of the full EMEC wheel) and one quarter of the full FCal1 and FCal2 detectors were assembled. The results of this scan for the performance of the EMEC, HEC and FCal on the electromagnetic scale are described in [154]. These results demonstrate that the response and resolution of electrons and pions across most of the EMEC/HEC and FCal acceptance, including the crack region around $\eta = 3.2$, show reasonable agreement with expectations from detailed simulation.

As an example, figure 5.41 shows the response on the electromagnetic scale for 200 GeV pions, when moving from the FCal region (left) across the crack to the EMEC/HEC region (right). Shown is the total energy response together with the individual responses in the different electro-

magnetic (FCal1 and EMEC) and hadronic (FCal2 and HEC) components of the calorimeter. For the energy reconstruction, a cone size of $\Delta R \times \Delta\phi = 0.30$ has been used. The data are compared with simulation (GEANT 4, version 7.1 with physics list QGSP-GN 2.6). The prediction for the total electromagnetic energy measured in the FCal region shows some deviations from the data. As already known from previous studies with the QGSP physics list, the simulation tends to predict too compact hadronic showers in comparison to the data. But the general loss of signal (on the electromagnetic scale), when traversing the crack region is not more than $\sim 20\%$. The details of the complex material structure in the crack region are rather well described in the simulation.

5.7.3 FCal performance

There have been two FCal stand-alone test-beam periods at the CERN SPS, one in 1998 and one in 2003. The 1998 period used engineering modules which were full-depth segments of FCal1 and FCal2. The electron response of FCal1 and an estimate of the electromagnetic scale for FCal2 were extracted from these measurements [155]. The 2003 test-beam was carried out with the final production modules and used electronics which were very similar to the final electronics implemented for ATLAS. Data were taken with electron and pion beams with momenta from 10 to 200 GeV. The data were analysed using the standard LAr technique of optimal filtering (see section 5.6.1.4). Electronic noise was calculated from the data and was subtracted in quadrature before energy resolution plots, such as those shown in figures 5.42 and 5.43, were produced.

Figures 5.42 and 5.43 illustrate the results obtained after subtraction of the electronic noise from the data. The points have been fitted with the function in eq. (5.2). The fit to the electron data in figure 5.42 yielded stochastic and constant terms of $(28.5 \pm 1.0)\% \sqrt{\text{GeV}}$ and $(3.5 \pm 0.1)\%$, respectively. For pions, the energy resolution depends on the technique used to correct the reconstructed energies from the electromagnetic scale to the hadronic scale. Two techniques were employed: the first one uses a single weight per module (flat weights) and yields stochastic and constant terms of $(94.2 \pm 1.6)\% \sqrt{\text{GeV}}$ and $(7.5 \pm 0.4)\%$, respectively. A more sophisticated technique, using radial weights, which exploits the fine transverse segmentation of the FCal, improves the sampling term from 94% to 70% and yields a constant term of 3.0%. The measured energy resolution for pions with an energy of 200 GeV is improved from 10.1% to 5.8% as shown in figure 5.43.

The resolutions obtained in these FCal beam tests meet well the design specifications, which were expressed as stochastic and constant terms of 100% and 10% respectively for hadrons. Further details of the results of the 2003 test-beam measurements can be found in [156].

5.7.4 Tile-calorimeter performance

5.7.4.1 Stand-alone performance

Approximately 12% of all production modules of the tile calorimeter have been measured extensively in dedicated test-beam periods at the CERN SPS.

Muons with an energy of 180 GeV and incident at 90° to the module symmetry plane were used to study the photo-electron yield for all eleven tile sizes in the detector (monitoring the photo-electron yield checks for any deterioration in time of the optical response of the calorimeter).

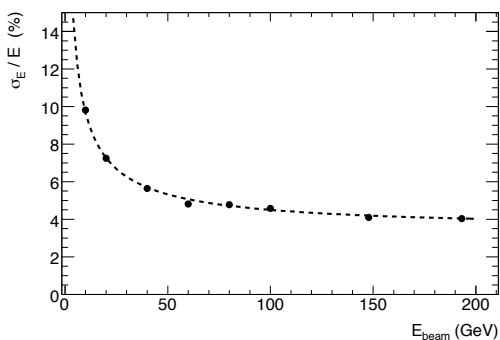


Figure 5.42: Fractional energy resolution obtained for electrons measured in the first module of the forward calorimeter as a function of the beam energy, E_{beam} . The curve corresponds to the result of a fit to the data points using eq. 5.2.

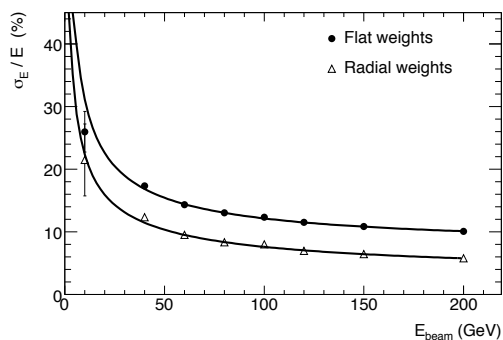


Figure 5.43: Fractional energy resolution obtained for pions, measured in all three modules of the forward calorimeter, as a function of the beam energy, E_{beam} . The data are shown for two cell-weighting schemes and the curves correspond to the result of a fit to the data points using eq. 5.2.

The photo-electron yield was calibrated using two independent techniques. The first one uses the spread in the difference of signals from the two photomultiplier tubes for muons passing through the centre of the cell. The second one uses the spread in the laser-generated light to calibrate the photomultiplier response in photo-electrons per pC and the measured signal for muons and electrons. The results of the two methods are in excellent agreement: the light yield is independent of the size of the tiles within 1–2% uncertainties. These results also reproduced the batch-to-batch light output variation seen during tile production, together with the systematic difference associated with the two sources of raw polystyrene (the photo-electron yield is about 80 per GeV for one source and about 100 per GeV for the other source). In the extended-barrel modules, the yield is 10% to 20% lower, reflecting the choice which was made to use batches with higher light yields for the barrel modules. The muon data at 90° incidence also provided the means to study the local and global features of the calorimeter response. The spread of the mean signals from the eleven tile sizes is 2.0% (respectively 2.8%) for the barrel (respectively extended-barrel) modules and the spread within each tile size is about 3%. The average response of a module varies between modules with a spread of 1.2%, while the variation within a given module is typically 4–5%.

The muon signal-to-noise ratios are very large, typically 44 when summing over a tower (three radial layers and over $\Delta\eta \times \Delta\phi \approx 0.1 \times 0.1$) and 18 in the last radial layer. This feature is expected to provide reliable identification of isolated muons down to energies of ~ 2 GeV even in the presence of pile-up noise, which is negligible in the last layer. The response to 180 GeV muons, averaging over angles in the range $-1.49 < |\eta| < 1.35$ has a spread of 1.9% (rms), excluding angles for which the coverage is not complete.

The modules were exposed to electron beams with energies between 10 and 180 GeV, to set the energy conversion scale (i.e. the photomultiplier high voltage to be supplied, as discussed in section 5.6.1.3) for a significant fraction of the cells of the entire module. The cesium system will be used to transfer this basic calibration to the majority of modules which were not calibrated using

high-energy beams. Electron showers are mostly contained in the first radial layer, therefore precise response values can only be extracted from this first layer of cells. The spread of these responses over the entire exposed module sample is up to 3%. The electron response is linear with deviations of about 1%. The electron response is observed to vary with the angle of incidence, as expected because of the variation in the effective calorimeter granularity with angle. Between extremes, corresponding to angles to the tile/steel plate planes from 0° to 90° , the response increases by approximately 8%.

Systematic measurements were performed using hadron beams with energies in the 20–180 GeV range, with a few additional runs at 350 GeV. The set-up consisted of a vertical stack of three modules, in which the production module under test occupied the central position. For hadrons incident on this module, transverse leakage of hadron showers is approximately 1%, while longitudinal leakage significantly affects the resolution particularly at higher energies and lower impact angles. The beams typically contained a mixture of pions, kaons and protons. The beam-line included a Cerenkov counter which was used to separate pions and protons in the case of positive beam energies (between 50 GeV and 180 GeV).

The fractional energy resolution, σ_E/E , for isolated pions was studied as a function of beam energy and impact angle. The results are summed at the electromagnetic scale over all cells and the resulting energy resolutions for $\eta = 0.35$ are shown in figure 5.44. The parametrisation of eq. (5.2) was used to fit the results and the best fit yields $a = (56.4 \pm 0.4)\%$ and $b = (5.5 \pm 0.1)\%$. The statistical errors quoted here do not display the correlation between the two terms. These results are in good agreement with earlier stand-alone measurements made with prototype modules, when accounting for the fact that the latter were radially longer by 1.5 interaction lengths in order to represent the total depth of electromagnetic and hadronic calorimetry.

The fractional energy resolution for production modules displays a significant dependence on η , mostly as a result of the increase in effective depth and decrease of longitudinal leakage as η increases. As representative examples, σ_E/E at $\eta = 0.25$ is $(14.2 \pm 0.1)\%$ at 20 GeV and $(6.6 \pm 0.1)\%$ at 350 GeV, whereas, at $\eta = 0.55$, σ_E/E is $(13.0 \pm 0.1)\%$ at 20 GeV and $(5.9 \pm 0.1)\%$ at 350 GeV. The module-to-module uniformity has been studied with 180 GeV pions entering the calorimeter under various impact points and incidence angles. The uniformity in the mean response was found to be independent of η over all modules measured in the test-beam and shows an average spread of 1.4% [157].

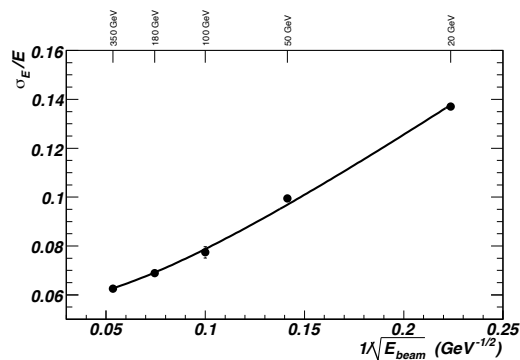


Figure 5.44: Fractional energy resolution obtained for pions as a function of the inverse square root of the beam energy at an angle of incidence equivalent to $|\eta| = 0.35$.

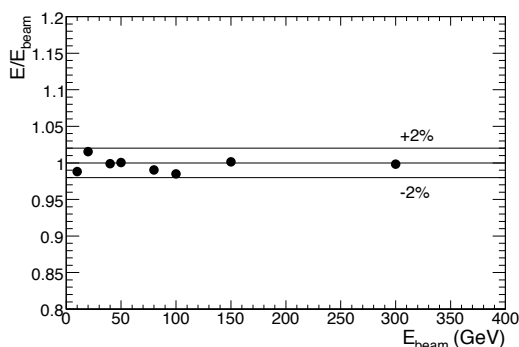


Figure 5.45: Linearity of response as a function of the pion beam energy, E_{beam} , for combined LAr and tile calorimetry at $|\eta| = 0.25$.

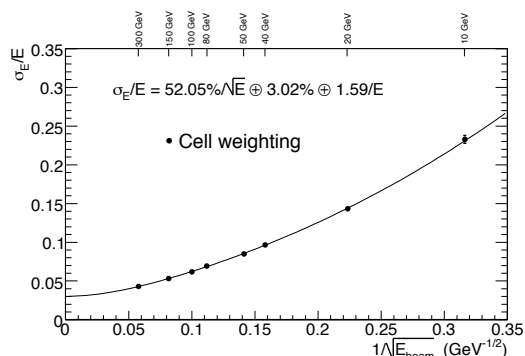


Figure 5.46: Fractional energy resolution obtained for pions as a function of the inverse square root of the beam energy, E_{beam} , for combined LAr and tile calorimetry at $|\eta| = 0.25$. The curve corresponds to the result of a fit to the data points with the functional form as shown.

5.7.4.2 Combined LAr and tile calorimeter test-beam measurements

The combined performance of the barrel LAr electromagnetic and tile calorimeters was measured in 1996 in the H8 beam at the CERN SPS. The set-up used prototype modules of the two calorimeters. The LAr stack consisted of two modules, each spanning nine degrees in the azimuthal direction. The modules were longitudinally segmented into three layers, of $9 X_0$, $9 X_0$ and $7 X_0$ each at $\eta = 0$, for a total of 25 radiation lengths (1.22 interaction lengths). The segmentation was 0.018×0.02 in $\Delta\eta \times \Delta\phi$ for the first two longitudinal layers and 0.036×0.02 for the third layer.

Five prototype modules of the tile calorimeter, each covering $\Delta\phi = 0.1$, were stacked vertically downstream of the LAr cryostat and as close as possible to it; the distance between the active parts of the two detectors was nevertheless about 55 cm, roughly twice as much as in ATLAS. The tile calorimeter modules had the same steel and scintillator plate geometry as the production modules, but, in the longitudinal direction, the active portion of the calorimeter measured 180 cm, rather than 152 cm as in the production modules. These modules were segmented into four longitudinal layers, of about 1.5, 2.0, 2.5 and 3 interaction lengths; in the η -direction, each module was segmented into five equal cells of size $\Delta\eta = 0.2$.

The hadron beam consisted of pions with an energy-dependent proton component and impinged on the combined calorimeter assembly at an angle of 12° . Data were taken in the energy range between 10 and 300 GeV. The pion energy was reconstructed by a cell-weighting technique, which corrected upwards the response of cells with relatively small signals to equalise it to that of cells with large, typically electromagnetic, signals. This method had been successfully tested in a combined LAr and tile calorimeter test-beam run, as described in [158]. The total energy is expressed as:

$$E = \sum_{\text{em.cells}} W_{\text{em}}(E_{\text{cell}}, E_{\text{beam}}) \cdot E_{\text{cell}} + \sum_{\text{had.cells}} W_{\text{had}}(E_{\text{cell}}, E_{\text{beam}}) \cdot E_{\text{cell}} + E_{\text{cryo}}$$
 where the last term accounts for the energy lost in the dead region between the electromagnetic and the hadronic

calorimeters and is taken to be proportional to the geometric mean of the energies deposited in the last electromagnetic layer and the first hadronic layer: $E_{\text{cryo}} = W_{\text{cryo}} \cdot \sqrt{E_{\text{em}_3} \cdot E_{\text{had}_1}}$

As a first step, the optimal weights for each readout cell and each beam energy are determined by minimising the energy resolution in a dozen cell energy bins, under the constraint that the mean reconstructed energy reproduces the nominal beam energy. A substantial reduction in the number of energy reconstruction parameters is then obtained by expressing the weights for any bin as simple functions of the cell energies: $w_{\text{em}} = a_E + b_E/E_{\text{cell}}$, $w_{\text{had}} = a_H + b_H/E_{\text{cell}}$, where the a and b coefficients are obtained specifically for each beam energy. As a second step, the dependence of the a and b coefficients on the beam energy is parametrised. At this point, all weights are expressed as a function of only eight parameters which include the weight corresponding to the cryostat term. A further step implements an energy reconstruction method which does not rely on a priori knowledge of the incident particle energy: a first-pass value of the total energy is calculated and used as the nominal value in minimising the resolution for the first-pass determination of the weights, according to the functional forms just described. The procedure is iterated until the reconstructed energy is stable.

In the procedure described here, the only information gained using a priori knowledge of the beam energy is the functional form of the weights, but their values are boot-strapped from the raw data. Using this algorithm, the linearity and resolution results in figures 5.45 and 5.46 are obtained [159]. The hadron response deviation from linearity is within $\pm 2\%$ over the entire beam-energy range. This is a consequence of the constraint applied in the first pass of the weight determination. The fractional energy resolution is well fitted by the sum in quadrature of a stochastic term of $(52.0 \pm 1.0)\%$, a constant term of $(3.0 \pm 0.1)\%$ and an electronic-noise term of $1.6 \text{ GeV} \pm 0.1\%$.